VERSION APRIL 28, 2026
Preprint typeset using LaTeX style openjournal v. 09/06/15

arXiv:2512.15960v3 [astro-ph.CO] 27 Apr 2026

DESI-DR1 3 × 2-PT ANALYSIS: CONSISTENT COSMOLOGY ACROSS WEAK LENSING SURVEYS

A. PORREDON [1,2,3,4] C. BLAKE [5] J. U. LANGE [6] N. EMAS,[5] J. AGUILAR,[7] S. AHLEN [8] A. BERA,[9] D. BIANCHI [10,11] D. BROOKS,[12] F. J. CASTANDER [13,14] T. CLAYBAUGH,[7] J. COLOMA NADAL,[15] A. CUCEU [7] K. S. DAWSON [16] A. DE LA MACORRA [17] BIPRATEEP DEY [18,19] P. DOEL,[12] A. ELLIOTT [20,4] S. FERRARO [7,21] A. FONT-RIBERA [22] J. E. FORERO-ROMERO [23,24] C. GARCIA-QUINTERO [25,26] E. GAZTAÑAGA [13,27,14] S. GONTCHO A GONTCHO [7,28] G. GUTIERREZ,[29] J. GUY [7] B. HADZHIYSKA [30,21] H. K. HERRERA-ALCANTAR [31,32] S. HEYDENREICH [33] K. HONSCHEID [34,20,4] C. HOWLETT [35] D. HUTERER [36,37] M. ISHAK [9] S. JOUDAKI [1] R. JOYCE [38] D. KIRKBY [39] A. KREMIN [7] A. KROLEWSKI,[40,41,42] O. LAHAV,[12] C. LAMMAN [4] M. LANDRIAU [7] L. LE GUILLOU [43] A. LEAUTHAUD [33,44] M. E. LEVI [7] M. MANERA [45,22] A. MEISNER [38] R. MIQUEL,[46,22] S. NADATHUR [27] J. A. NEWMAN [19] G. NIZ [47,48] N. PALANQUE-DELABROUILLE [32,7] W. J. PERCIVAL [40,41,42] C. POPPETT,[7,49,21] F. PRADA [50] I. PÉREZ-RÀFOLS [51] A. ROBERTSON,[38] G. ROSSI,[52] R. RUGGERI [53] E. SANCHEZ [1] C. SAULDER [54] D. SCHLEGEL,[7] M. SCHUBNELL,[36,37] A. SEMENAITE,[5] H. SEO [55] J. SILBER [7] A. SOUKI,[1] D. SPRAYBERRY,[38] G. TARLÉ [37] M. VARGAS-MAGAÑA [17] B. A. WEAVER,[38] C. ZHOU,[33] R. ZHOU [7] AND H. ZOU [56]

(DESI COLLABORATION)

(Affiliations can be found after the references)

Version April 28, 2026

ABSTRACT

We present a joint cosmological analysis of projected galaxy clustering observations from the Dark Energy Spectroscopic Instrument Data Release 1 (DESI-DR1), and overlapping weak gravitational lensing observations from three datasets: the Kilo-Degree Survey (KiDS-1000), the Dark Energy Survey (DES-Y3), and the Hyper-Suprime-Cam Survey (HSC-Y3). This combination of large-scale structure probes allows us to measure a set of 3×2-pt correlation functions, breaking the degeneracies between parameters in cosmological fits to individual observables. We obtain mutually-consistent constraints on the parameter $S_8 = \sigma_8\sqrt{\Omega_{\rm m}/0.3} = 0.786^{+0.022}_{-0.019}$ from the combination of DESI-DR1 and DES-Y3, $S_8 = 0.760^{+0.020}_{-0.018}$ from KiDS-1000, and $S_8 = 0.771^{+0.026}_{-0.027}$ from HSC-Y3. These parameter determinations are consistent with fits to the *Planck* Cosmic Microwave Background dataset, albeit with $1.5 - 2\sigma$ lower values in the $S_8 - \Omega_{\rm m}$ plane. We perform our analysis with a unified pipeline tailored to the requirements of each cosmic shear survey, which self-consistently determines cosmological and astrophysical parameters. We generate an analytical covariance matrix for the correlation data including all cross-covariances between probes, and we design a new blinding procedure to safeguard our analysis against confirmation bias, whilst leaving goodness-of-fit statistics unchanged. Our study is part of a suite of papers that present joint cosmological analyses of DESI-DR1 and weak gravitational lensing datasets.

Keywords: Cosmology, weak gravitational lensing, large-scale structure of Universe

1. INTRODUCTION

A central goal of modern cosmology is to define and scrutinise the model that describes the composition, initial conditions and evolution of the Universe. Given a set of compelling unsolved problems, including the unknown physics represented by dark matter and dark energy, we seek new information that might refine our knowledge (for reviews, see Weinberg et al. 2013; Ishak 2019; Moresco et al. 2022; Huterer 2023). As cosmological datasets continue to expand impressively, an important theme is to combine these datasets in unified analysis frameworks. Such joint analyses serve to improve the statistical precision of our cosmological parameter determinations, mitigate against key systematic errors, and stress-test the self-consistency of our model framework against the baseline established by analyses of the Cosmic Microwave Background (CMB) radiation (Planck Collaboration et al. 2020). Such comparisons have already revealed a variety of "tensions" and "intriguing hints" which guide future exploration: including disagreements between determinations of the local expansion rate (Riess et al. 2016; Di Valentino et al. 2021; Freedman 2021; Riess et al. 2022; Vagnozzi 2023), debates over the amplitude of matter fluctuations (Leauthaud et al. 2017; Joudaki et al. 2018; Heymans et al. 2021), and suggestions that the physics of dark energy might evolve with time (DESI Collaboration et al. 2025a,b,c).

The large-scale structure of the Universe as mapped by spectroscopic redshift surveys, and the gravitational lensing of light by this structure as probed by photometric imaging surveys, have long been seen as highly complementary cosmological probes (e.g., Cai & Bernstein 2012; Gaztañaga et al. 2012; de Putter et al. 2013; Kirk et al. 2015). A set of 3×2-pt correlation statistics can be constructed from these datasets: cosmic shear, the correlated distortions in galaxy shapes induced by weak gravitational lensing by the cosmic web; galaxy clustering, the correlations between galaxy positions caused by gravitational physics; and galaxy-galaxy lensing, the tangential shear of background source galaxies around foreground lens galaxies. The amplitude and scale-dependence of these correlations may be accurately predicted by lensing and clustering theory, allowing us to infer the values of the cosmological parameters which control the expansion, growth and distribution of matter. However, correlations

*E-mail: annamaria.porredon@ciemat.es

are also induced by a variety of astrophysical effects, including intrinsic alignments, unknown photometric redshift distributions, baryonic effects in the matter power spectrum, shape measurement calibrations, and the biasing of galaxies with respect to matter fluctuations. Testing the cosmological model in light of these potential complications requires us to create a joint analysis framework which can be applied across survey datasets.

In this paper, we present a unified cosmology analysis of $3\times$ 2-pt statistics utilising the large-scale structure dataset assembled by the Dark Energy Spectroscopic Instrument (DESI) in conjunction with three important weak lensing (WL) surveys. We hence use DESI galaxies to form the lens sample for the 3×2-pt correlations, instead of photometric galaxies from the imaging surveys. DESI, which has been operating its main survey program at Kitt Peak National Observatory since 2021, has already assembled the largest existing spectroscopic redshift dataset for cosmology, exceeding previous programs by more than an order of magnitude (DESI Collaboration et al. 2016a,b, 2024). Our study is based on the first substantial assembly of DESI data, compiled from the first year of operations (Data Release 1, DESI Collaboration et al. 2026). Together with DESI data, we also use publicly-available weak lensing catalogues from the Dark Energy Survey Year 3 (DES-Y3, Sevilla-Noarbe et al. 2021; Gatti et al. 2021), the Kilo-Degree Survey (KiDS-1000, Kuijken et al. 2019; Giblin et al. 2021), and the Hyper Suprime-Cam survey Year 3 (HSC-Y3, Aihara et al. 2022; Li et al. 2022). Our work builds upon a wealth of cosmological studies already presented by these collaborations (e.g., Hildebrandt et al. 2017; DES Collaboration 2018; Hikage et al. 2019; Hamana et al. 2020; Hildebrandt et al. 2020; Heymans et al. 2021; DES Collaboration 2022; Li et al. 2023; Dalal et al. 2023; Wright et al. 2025). In particular, DES and KiDS Collaboration (2023); García-García et al. (2024); Jefferson et al. (2025) have previously performed analyses under a unified modelling pipeline.

Our work presents several key advances in the 3×2-pt cosmology program. First, DESI-DR1 provides an unprecedented set of new spectroscopic lenses, overlapping with all the weak lensing surveys considered in our study and hence allowing the measurement of consistent galaxy-galaxy lensing cross-correlations. Second, spectroscopic clustering samples allow the usage of the projected correlation function $w_p(r_p)$ for the lens auto-correlations, rather than the angular correlations $w(\theta)$ that are accessible in photometric datasets. The projected correlation function can be measured with higher signal-to-noise ratio than $w(\theta)$, since the signal is integrated over a narrower radial extent, and hence experiences less dilution. As a third aspect, our work has extended 3×2-pt analytical covariance frameworks to include $w_p(r_p)$ rather than $w(\theta)$. Finally, we have created a new unified analysis pipeline, tailored to the requirements of each cosmic shear survey, which self-consistently determines cosmological and astrophysical parameters.

The current paper is the culmination of a set of preparatory studies which have tested and validated the different components of our analysis. Blake et al. (2025) presented a "mock challenge" study of simulated catalogues representing our key datasets. Yuan et al. (2024) tested our selection of lens galaxies from the parent DESI dataset and the associated covariance for galaxy-galaxy lensing, and Heydenreich et al. (2025) presented galaxy-galaxy measurements for our weak lensing survey sources and tested their consistency. Emas et al. (2026) performed validation of the scale cuts used in this study, and used shear ratios to test for the presence of systematic effects in lensing amplitudes, and Ruggeri et al. (2025) analysed the position cross-correlations between the lensing and DESI catalogues to validate the source redshift distributions via the clustering-redshift technique. As companion papers to our work, Semenaite et al. (2025) and DeRose et al. (2026) present joint cosmological analyses of lensing and clustering multipoles which include the effect of redshift-space distortions, in contrast to the projected clustering statistic adopted in our study, and Lange et al. (2025b) present full-scale analyses of galaxy-galaxy lensing and clustering statistics using emulators calibrated by simulations, which permit models to be extended to smaller scales than utilised in our study.

Our paper is structured as follows: in Sec. 2 we overview the large-scale structure and weak lensing datasets used in this study. In Sec. 3 we describe our methodology for modelling and measuring the 3×2-pt correlations, for determining the covariance of the statistics, and for applying the data-vector blinding we implement to mitigate against confirmation bias. In Sec. 4 we describe our cosmological results and robustness tests, and in Sec. 5 we compare our results with other studies. We conclude our work in Sec. 6.

2. DATA

2.1. *DESI Data Release 1*

The Dark Energy Spectroscopic Instrument (DESI) is a multi-object spectrograph installed at the 4-metre Mayall Telescope at Kitt Peak National Observatory. Over its 8-year main survey program, which commenced in May 2021, DESI will collect over 60 million spectra of galaxies and quasars across $17{,}000\,\deg^2$ (DESI Collaboration et al. 2016a,b, 2024), increasing the size of existing large-scale structure samples by more than an order-of-magnitude. The instrument design is described by DESI Collaboration et al. (2022), including an optical corrector (Miller et al. 2024) and a robotic positioner (Silber et al. 2023) that can assign up to 5000 fibres to targets in the focal plane (Poppett et al. 2024), where the resulting data are processed by the DESI spectroscopic pipeline (Guy et al. 2023). In the DESI observing strategy, described by Schlafly et al. (2023), the survey obtains spectra for four principal target classes, photometrically-selected from the DESI Legacy optical imaging surveys (Dey et al. 2019): these components are called the Bright Galaxy Survey (BGS, Hahn et al. 2023), Luminous Red Galaxy Survey (LRG, Zhou et al. 2023), Emission Line Galaxy Survey (ELG, Raichoor et al. 2023), and Quasar Survey (QSO, Chaussidon et al. 2023).

We use DESI Data Release 1 (DR1, DESI Collaboration et al. 2026) as the dataset for the galaxy-galaxy lensing and galaxy clustering measurements in this analysis. DESI-DR1 consists of all data acquired during the first 13 months of the main survey up to June 2022, including high-confidence redshifts for 13.1M galaxies (DESI Collaboration et al. 2026). In our analysis we use catalogues from the Bright Galaxy Survey (Hahn et al. 2023) and Luminous Red Galaxy survey (Zhou et al. 2023). Bright Galaxies span redshift range $0.1 < z < 0.4$, which we divide into three narrower redshift ranges $(0.1 - 0.2, 0.2 - 0.3, 0.3 - 0.4)$. Within each of these BGS redshift bins, we apply luminosity cuts to select lens samples (Yuan et al. 2024), which we use for galaxy-galaxy lensing and clustering measurements (Heydenreich et al. 2025). In our study, we hence select fainter BGS samples than utilised for the Key Project Baryon Acoustic Oscillation and full shape analyses (DESI Collaboration et al. 2025d,e), to increase the signal-to-noise of the resulting galaxy-galaxy lensing measurements (Yuan et al. 2024). To these three BGS lens samples, we add LRG catalogues in redshift ranges $(0.4 - 0.6, 0.6 - 0.8)$, which are the same samples as used in the DESI Key Project. We do not use the $0.8 < z < 1.1$ LRG sample in our study, because of its poor efficiency for lensing with current weak lensing surveys (and we also do not utilise the higher-redshift DESI Emission Line Galaxy and Quasar samples for the same reason).

2.2. *DES Year 3*

In addition to the DESI spectroscopic large-scale structure dataset, we employ weak gravitational lensing shear measurements from three current photometric imaging surveys. First, we include the Dark Energy Survey Year 3 (DES-Y3) shear catalogue (Gatti et al. 2021) in our analysis. The Dark Energy Survey has used the Dark Energy Camera mounted on the Blanco 4-metre Telescope (Flaugher et al. 2015) to conduct the largest existing weak lensing survey. The DES-Y3 catalogue, which contains more than 10^8 objects over $4{,}143$ deg^2, was based on imaging data from the first three years of DES operation between 2013 and 2016 (Sevilla-Noarbe et al. 2021). The shear catalogue was created from this imaging dataset using the self-calibrating shear measurement pipeline METACALIBRATION (Sheldon & Huff 2017), and further re-calibrated for shear bias and blending by a suite of image simulations (MacCrann et al. 2022), and has a weighted source number density of 5.6 arcmin^{-2} and corresponding shape noise $\sigma_e = 0.26$. We analysed DES-Y3 sources in the four tomographic bins created by the collaboration (Myles et al. 2021), split by photometric redshifts $[0.00, 0.36, 0.63, 0.89, 2.00]$. The DES collaboration has performed validations and cosmological fits based on these catalogues (see, DES Collaboration 2022; Secco et al. 2022; Amon et al. 2022). We note that, in our analysis, we use a revised version of the DES-Y3 catalogue with updated source tomographic bin assignments, matching the current files available in the DES-Y3 data release page[1] (see also footnote 5 of McCullough et al. 2024). The DES-Y3 catalogue has an overlap of 851.3 deg^2 with the DESI-DR1 footprint.

2.3. *KiDS-1000*

The second weak lensing dataset we include in our analysis is the Kilo-Degree Survey (KiDS-1000) weak lensing catalogue (Giblin et al. 2021), which is part of the fourth public KiDS data release (Kuijken et al. 2019). KiDS has utilised the OmegaCAM instrument on the Very Large Telescope Survey Telescope (VST) at the Paranal Observatory to image the sky in optical filters u, g, r, i. Complementary imaging in the near-infrared bands Z, Y, J, H, K_s has been obtained by the VISTA-VIKING survey, resulting in a deep, wide, nine-band imaging dataset with improved photometric redshift calibration (Hildebrandt et al. 2021). KiDS-1000 includes $1{,}006$ deg^2 of lensing data, consisting of 21 million galaxies with an effective number density 6.2 arcmin^{-2}, with source shapes measured using the *lens*fit model fitting technique (Miller et al. 2013; Fenech Conti et al. 2017). Our analysis uses the five tomographic source samples defined by KiDS, which are divided by photometric redshifts $[0.1, 0.3, 0.5, 0.7, 0.9, 1.2]$, where the redshift distribution of the sources is calibrated as described by Hildebrandt et al. (2021). Cosmological fits to the KiDS-1000 dataset were presented by Heymans et al. (2021), and joint cosmological analyses of DES-Y3 and KiDS-1000 have been performed by DES and KiDS Collaboration (2023). The area of overlap of KiDS-1000 and DESI-DR1 is 446.8 deg^2. Whilst our work was in progress, cosmological analysis of the extended KiDS-Legacy survey was presented by that collaboration (Wright et al. 2025).

2.4. *HSC Year 3*

The third and final weak lensing dataset we include in our study is the Hyper Suprime-Cam survey Year 3 catalogue (HSC-Y3 Li et al. 2022). The HSC survey is using the 8.2-metre Subaru Telescope to create the deepest large-scale weak lensing dataset currently available, imaging several regions of sky in g, r, i, z, Y filters, where the i-band seeing is around $0.6''$ (Aihara et al. 2022). The HSC-Y3 catalogue is based on data acquired between 2014 and 2019, covering 434 deg^2 of sky with effective source density 19.9 arcmin^{-2}. The catalogue is based on source shape measurements performed using a re-Gaussianization PSF correction method (Mandelbaum et al. 2018), further calibrated by realistic image simulations that emulate survey observation conditions (Li et al. 2022). Our work uses the four tomographic source samples defined by the HSC collaboration, with photometric redshift divisions $[0.3, 0.6, 0.9, 1.2, 1.5]$, and redshift distributions inferred by Rau et al. (2023). Cosmological fits to these datasets have been presented by Li et al. (2023) and Dalal et al. (2023). We note that, recently, Choppin de Janvry et al. (2025a,b) produced an updated calibration of the HSC-Y3 redshift distributions using spectroscopic data from DESI DR1 and DR2 that was not available in Rau et al. (2023). In this work, we use the original redshift distributions from Rau et al. (2023) and the priors from the fiducial HSC-Y3 analyses (Li et al. 2023; Dalal et al. 2023) (see Sec. 3.3 for details). The HSC-Y3 dataset has almost complete overlap with DESI-DR1. Sky coverage maps of the different datasets used in our analysis can be found in Fig. 1 of Emas et al. (2026).

3. METHODOLOGY

In this section we describe our methodology for inferring cosmological parameters from the combination of DESI-DR1 galaxy clustering data and DES, KiDS, and HSC weak lensing data. We assume two main cosmological models: flat ΛCDM and flat wCDM, with w being the equation of state for dark energy, which we assume is constant in time.

We fit these cosmological models to a combination of 3×2-pt configuration-space correlation measurements generated from the galaxy source and lens samples as described in Sec. 3.2. We use the cosmic shear correlation functions for the tomographic source sub-samples of the weak lensing surveys, $\xi_{\pm}(\theta)$, as a function of angular separation θ; the projected galaxy correlation functions of each DESI lens sample, $w_p(r_p)$, as a function of projected separation r_p; and the average tangential shear of the source samples around the lens galaxies, $\gamma_t(\theta)$. For the lens clustering, we note that we utilise the projected correlation function in preference to the angular correlation function, $w(\theta)$, since $w_p(r_p)$ can be measured with a higher signal-to-noise ratio (S/N) than $w(\theta)$ for spectroscopic lens samples. Heydenreich et al. (2025) also provides measurements of the excess surface mass density $\Delta\Sigma(r_p)$ for galaxy-galaxy lensing. Nevertheless, we opt to stick with $\gamma_t(\theta)$ because the S/N gain is not as clear in this case (Shirasaki & Takada 2018), and this allows us to use the modelling framework from DES Collaboration (2022).

[1] https://des.ncsa.illinois.edu/releases/y3a2/Y3key-catalogs

3.1. *Modelling*

3.1.1. *Cosmic shear*

We follow the DES-Y3 framework described in Krause et al. (2021) and DES Collaboration (2022) to model the angular two-point correlation functions of cosmic shear and galaxy-galaxy lensing. For cosmic shear, and for two given redshift bins i and j, these functions can be expressed in terms of the convergence angular power spectrum $C_\kappa(\ell)$ at an angular wavenumber ℓ:

$$\xi_\pm^{ij}(\theta) = \sum_\ell \frac{2\ell+1}{2\pi\ell^2(\ell+1)^2}\left[G^+_{\ell,2}(\cos\theta) \pm G^-_{\ell,2}(\cos\theta)\right] \times \left[C^{ij}_{\kappa,\mathrm{EE}}(\ell) \pm C^{ij}_{\kappa,\mathrm{BB}}(\ell)\right], \tag{1}$$

where $G_\ell^\pm$ are computed from the Legendre polynomials P_ℓ (see Eq. (4.19) of Stebbins (1996) for their full expression). The two-point correlation functions are then averaged over each angular bin $[\theta_{\rm min}, \theta_{\rm max}]$ following the expressions from Fang et al. (2020a). The observed shear angular power spectra can be decomposed into E and B modes, with the B-mode contribution $C^{ij}_{\kappa,\mathrm{BB}}(\ell)$ originating from the intrinsic alignments of galaxies (see e.g. Troxel & Ishak 2015 and Lamman et al. 2024 for reviews):

$$C^{ij}_{\kappa,\mathrm{EE}}(\ell) = C^{ij}_{\kappa\kappa}(\ell) + C^{ij}_{\kappa \mathrm{I_E}}(\ell) + C^{ji}_{\kappa \mathrm{I_E}}(\ell) + C^{ij}_{\mathrm{I_E I_E}}(\ell), \tag{2}$$

$$C^{ij}_{\kappa,\mathrm{BB}}(\ell) = C^{ij}_{\mathrm{I_B I_B}}(\ell), \tag{3}$$

where I denotes an intrinsic alignment contribution.

The angular convergence power spectrum $C_{\kappa\kappa}(\ell)$ can be obtained from the non-linear 3D matter power spectrum $P_{\rm mm}$. Under the Limber approximation (Limber 1953; LoVerde & Afshordi 2008) and assuming a flat spatial geometry,

$$C^{ij}_{\kappa\kappa}(\ell) = \int_0^{\chi_{\rm H}} \mathrm{d}\chi \frac{W^i_\kappa(\chi) W^j_\kappa(\chi)}{\chi^2} P_{\rm mm}\left(\chi, k=\frac{\ell+1/2}{z(\chi)}\right), \tag{4}$$

where $\chi_{\rm H}$ is the horizon distance, $z(\chi)$ is the redshift at the comoving distance χ, and $W^i_\kappa(\chi)$ is the lensing efficiency kernel for the redshift bin i,

$$W^i_\kappa(\chi) = \frac{3H_0^2\Omega_{\rm m}}{2c^2}\frac{\chi}{a(\chi)}\int_\chi^{\chi_{\rm H}} \mathrm{d}\chi' n^i_{\rm s}(\chi')\frac{\chi'-\chi}{\chi'}, \tag{5}$$

with c being the speed of light, a the scale factor, H_0 the Hubble constant, $\Omega_{\rm m}$ the matter energy density, and $n^i_{\rm s}$ the normalized redshift distribution of source galaxies in bin i. We calculate the matter power spectrum $P_{\rm mm}$ from the CAMB (Lewis et al. 2000) implementation in COSMOSIS[2] (Zuntz et al. 2015), and we use HMCODE2020 with baryonic feedback (Mead et al. 2021) as our baseline model for the non-linear matter power spectrum.

For the intrinsic alignments, we assume the non-linear linear-alignment (NLA) model (Bridle & King 2007) as fiducial, since it has been widely used in previous weak lensing analyses (see, e.g., Asgari et al. 2021; DES Collaboration 2022; Miyatake et al. 2023; Wright et al. 2025; Anbajagane et al. 2025b) and is the fiducial choice in the joint cosmological analysis of DES-Y3 and KiDS-1000 cosmic shear (DES and KiDS Collaboration 2023). This model describes the linear tidal alignment of galaxies with the density field (Hirata & Seljak 2004) and includes an "ad hoc" non-linear correction to the linear matter power spectrum, as motivated by intrinsic alignment measurements in the Sloan Digital Sky Survey (Hirata et al. 2007). The NLA intrinsic alignment power spectra $C_{\kappa\mathrm{I_E}}(\ell)$ and $C_{\mathrm{I_E I_E}}(\ell)$ from Eq. (2) are described in Eqs. (3-5) in Bridle & King (2007), while $C_{\mathrm{I_B I_B}}(\ell) = 0$. With this model, the convergence-intrinsic and intrinsic-intrinsic power spectra are related to the nonlinear matter power spectrum through a redshift-dependent amplitude,

$$P_{\kappa\mathrm{I_E}} = c(z)P_{\rm mm}, \quad P_{\mathrm{I_E I_E}} = c^2(z)P_{\rm mm}, \tag{6}$$

$$c(z) = -A_{\rm IA}\frac{\bar{C}\rho_{\rm c}\Omega_{\rm m}}{D(z)}\left(\frac{1+z}{1+z_0}\right)^{\eta_{\rm IA}}, \tag{7}$$

where $D(z)$ is the growth function, $\rho_{\rm c}$ is the critical density, $z_0 = 0.62$ is the pivot redshift, and $\bar{C} = 5\times10^{-14} M_\odot h^{-2}\mathrm{Mpc}^2$ is obtained from SuperCOSMOS (Brown et al. 2002). $A_{\rm IA}$ and $\eta_{\rm IA}$ are free parameters that we vary in our analysis (see Sec. 3.3 for more details).

In some cases, we also consider the Tidal Alignment and Tidal Torquing model (TATT, Blazek et al. 2019), which extends the linear alignment model with the tidal torquing alignment mechanism. With this model, we have five free nuisance parameters: the tidal alignment amplitude, A_1, with redshift evolution η_1; the tidal torquing amplitude, A_2, with redshift evolution η_2, and a linear bias amplitude $b_{\rm TA}$. See Eqs. (37-39) in Blazek et al. 2019 for the expressions of the TATT intrinsic alignment power spectra, including a non-zero B-mode contribution $C_{\mathrm{I_B I_B}}(\ell)$. In the limit where $A_2, \eta_2, b_{\rm TA} \to 0$, the TATT model reduces to the NLA model, where A_1 and η_1 correspond to $A_{\rm IA}$ and $\eta_{\rm IA}$, respectively.

3.1.2. *Galaxy-galaxy lensing*

Similarly to cosmic shear, the galaxy-galaxy lensing two-point correlation function $\gamma_{\rm t}^{ij}$ for lens bin i and source bin j can be expressed in terms of the density-convergence angular power spectrum $C^{ij}_{\delta_{\rm g},\kappa}(\ell)$ as,

$$\gamma_{\rm t}^{ij}(\theta) = \sum_\ell \frac{2\ell+1}{4\pi\ell(\ell+1)} P^2_\ell(\cos\theta)\, C^{ij}_{\delta_{\rm g}\kappa_{\rm tot}}(\ell), \tag{8}$$

with P^2_ℓ being the Legendre polynomials, which are averaged over each angular bin in the same way as $\xi_\pm$, following Fang et al. (2020a). The observed density-convergence angular power spectrum also includes cross-terms related to intrinsic alignments ($\mathrm{I_E}$) and lens magnification ($\delta_{\rm mag}$),

$$C^{ij}_{\delta_{\rm g},\kappa_{\rm tot}}(\ell) = C^{ij}_{\delta_{\rm g}\kappa}(\ell) + C^{ij}_{\delta_{\rm g}\mathrm{I_E}}(\ell) + C^{ij}_{\delta_{\rm mag},\kappa}(\ell) + C^{ij}_{\delta_{\rm mag},\mathrm{I_E}}(\ell). \tag{9}$$

Under the Limber approximation and assuming a flat spatial geometry we obtain,

$$C^{ij}_{\delta_{\rm g}\kappa}(\ell) = \int_0^{\chi_{\rm H}} \mathrm{d}\chi \frac{W^i_{\delta_{\rm g}}(\chi) W^j_\kappa(\chi)}{\chi^2} P_{\rm mm}\left(\chi, k=\frac{\ell+1/2}{z(\chi)}\right), \tag{10}$$

with $W^i_{\delta_{\rm g}}(\chi)$ being the density kernel in lens redshift bin i,

$$W^i_{\delta_{\rm g}}(\chi) = b^i(z(\chi))\, n^i_{\rm l}(z(\chi))\, \frac{\mathrm{d}z}{\mathrm{d}\chi}, \tag{11}$$

where b^i is the galaxy bias and $n^i_{\rm l}(\chi)$ is the normalised redshift distribution of galaxies in lens bin i. In our analysis, we

[2] https://cosmosis.readthedocs.io

assume a linear galaxy bias model with one free parameter b^i per lens redshift bin i.

Lens magnification is an effect produced by gravitational lensing that impacts the number of galaxies observed in a given area of the sky. For galaxy-galaxy lensing, this effect is particularly important when the lens galaxies are behind the sources (see, e.g., Cross & Sánchez 2024 and Elvin-Poole, MacCrann et al. 2023). The effect of magnification on the projected number density contrast at position $\hat{\mathbf{n}}$ and redshift bin i can be expressed in terms of the convergence $\kappa^i(\hat{\mathbf{n}})$ experienced by lens galaxies in bin i,

$$\delta^i_{\rm mag}(\hat{\mathbf{n}}) = C^i\,\kappa^i(\hat{\mathbf{n}}), \tag{12}$$

where C^i is a constant of proportionality given by the response of the number of selected objects per area to a change in κ. This constant can be obtained from the measured slope of the luminosity function α^i at the faint end of the lens galaxy distribution in redshift bin i (Joachimi & Bridle 2010): $C^i = 2(\alpha^i - 1)$. We assume for α^i the values provided for our lens redshift bins in Table 3 of Heydenreich et al. (2025).

Given that the tangential shear two-point correlation function $\gamma_{\rm t}$ is a non-local measure of the galaxy-mass cross-correlation function, we follow MacCrann et al. (2020) and analytically marginalise over the mass enclosed below the angular scales included in the analysis. The analytical marginalisation is implemented by modifying the inverse of the covariance matrix when calculating the likelihood. We use the implementation and priors from the DES-Y3 analysis, which are described in detail in Pandey et al. (2022).

3.1.3. *Projected galaxy clustering*

As mentioned, we take advantage of the spectroscopic data from DESI and use the projected galaxy clustering correlation function $w_p(r_p)$, instead of the angular correlation function $w(\theta)$. We first follow Kaiser (1987) to obtain the redshift-space galaxy power spectrum from the matter power spectrum $P_{\rm mm}$, as a function of the Fourier modes k and the cosine of the angle between the direction of the wavevector and the line of sight, μ,

$$P_{\rm gg}(k,\mu) = b^2\,(1+\beta\mu^2)^2\,P_{\rm mm}(k), \tag{13}$$

with $\beta \equiv f/b$, where f is the logarithmic derivative of the growth factor $D(z)$ and b is the linear bias factor. $P_{\rm gg}(k,\mu)$ can then be expanded into Legendre polynomials of order 0, 2, and 4,

$$\begin{aligned} P_{\rm gg,0}(k) &= b^2\left(1+\frac{2}{3}\beta+\frac{1}{5}\beta^2\right)P_{\rm mm}(k),\\ P_{\rm gg,2}(k) &= b^2\left(\frac{4}{3}\beta+\frac{4}{7}\beta^2\right)P_{\rm mm}(k),\\ P_{\rm gg,4}(k) &= b^2\left(\frac{8}{35}\beta^2\right)P_{\rm mm}(k). \end{aligned} \tag{14}$$

From these power spectrum multipoles, we can obtain the correlation function multipoles $\xi_\ell(s)$ through a Hankel transform (Cole et al. 1994),

$$\xi_{{\rm gg},\ell}(s) = i^\ell\,\frac{1}{2\pi^2}\int_0^\infty {\rm d}k\,k^2\,P_{{\rm gg},\ell}(k)\,j_\ell(ks), \tag{15}$$

where s is the separation between two galaxies and $j_\ell(ks)$ is the spherical Bessel function of order ℓ. We can decompose s into perpendicular, r_p, and parallel, r_π, components to the line of sight: $s = \sqrt{r_p^2 + r_\pi^2}$. The projected correlation function $w_p(r_p)$ is then defined as the projection of $\xi_{\rm gg}(r_p, r_\pi)$ along the line of sight component,

$$w_p(r_p) = 2\int_0^{r_{\pi,\rm max}} {\rm d}r_\pi\,\xi_{\rm gg}(r_p, r_\pi), \tag{16}$$

where we assume $r_{\pi,\rm max} = 100\,h^{-1}{\rm Mpc}$ for the integration limit, matching the choice in the correlation measurement described below, and $\xi_{\rm gg}(r_p, r_\pi)$ is obtained from the sum of the correlation function multipoles from Eq. (15), weighted by the corresponding Legendre polynomials of order 0, 2 and 4.

We use the HANKL[3] package (Karamanis & Beutler 2021) to evaluate the Hankel transform of Eq. (15) with the FFTlog algorithm. As in the previous subsections, we use HMCODE2020 for the non-linear matter power spectrum $P_{\rm mm}$, and assume a linear galaxy bias model with one free parameter b^i per lens redshift bin i.

3.2. *Measurements*

In this section we briefly describe how we obtain or perform each correlation measurement. For the cosmic shear correlation functions between the tomographic source sub-samples of each weak lensing survey, we use the publicly-released measurements of the DES-Y3, KiDS-1000 and HSC-Y3 collaborations. DES-Y3 has presented $\xi_\pm(\theta)$ measurements in 20 logarithmically-spaced separation bins in the range $2.5 < \theta < 250'$ (DES Collaboration 2022); KiDS-1000 used 9 separation bins between limits $0.5 < \theta < 300'$ (Asgari et al. 2021); and HSC-Y3 performed cosmic shear measurements using 7 angular bins in the range $7.1 < \theta < 56.6'$ for ξ_+, and 7 bins in the range $31.2 < \theta < 248'$ for ξ_- (Li et al. 2023).

Our measurements of the projected galaxy correlation functions of the five DESI-DR1 lens samples, within redshift ranges $(0.1-0.2, 0.2-0.3, 0.3-0.4, 0.4-0.6, 0.6-0.8)$, are described by Heydenreich et al. (2025). In brief, the correlation function measurements were performed using PYCORR[4], which wraps a modified version of the CORRFUNC package[5] (Sinha & Garrison 2020). We performed measurements in 15 logarithmic separation bins in the range $0.08 < r_p < 80\,h^{-1}{\rm Mpc}$, where we will later exclude small separations which present modelling difficulties (see Sec. 3.5). When constructing the projected correlation function, we sum over line-of-sight separations $|r_\pi| \le 100\,h^{-1}{\rm Mpc}$ (choosing this limit to exceed the maximum value of r_p adopted). Our clustering measurements utilise accompanying DESI random catalogues (DESI Collaboration et al. 2025d), and employ weights which compensate for target selection systematics, spectroscopic incompleteness and fibre collisions. However, we exclude small-scale PIP (pairwise inverse probability) weights (Bianchi et al. 2025), because their effect is negligible at the separations relevant for our study. We also apply integral constraint corrections to the $w_p(r_p)$ measurements.

Finally, we measured the average tangential shear of all the tomographic source sub-samples around each DESI lens dataset. Our galaxy-galaxy lensing measurements using these catalogues are again discussed by Heydenreich et al. (2025). We correct our lensing measurements for multiplicative shear bias and dilutions due to source photometric redshift errors,

[3] https://hankl.readthedocs.io/
[4] https://py2pcf.readthedocs.io/
[5] https://corrfunc.readthedocs.io/

Table 1. Cosmological and astrophysical parameters, and their priors, used in the ΛCDM and wCDM analyses. The parameter w is fixed to -1 in ΛCDM. Square brackets denote a flat prior, while parentheses denote a Gaussian prior of the form $\mathcal{N}(\mu, \sigma)$.

Parameter	Fiducial	Prior
	Cosmology	
$\Omega_{\rm m}$	0.31	[0.1, 0.9]
$A_{\rm s}10^9$	2.08	[0.5, 5.0]
$n_{\rm s}$	0.96	[0.87, 1.07]
w	-1.0	[-2, -0.33]
$\Omega_{\rm b}$	0.049	[0.03, 0.07]
h_0	0.67	[0.55, 0.91]
$\Sigma\, m_\nu$ [eV]	0.06	[0.0, 0.6]
	Linear galaxy bias	
b^i	$1.35, 1.51, 1.65, 2.21, 2.44$	[0.8,4.0]
	Lens magnification	
α^1	0.94	$(0.94, 0.010)$
α^2	1.62	$(1.62, 0.010)$
α^3	2.19	$(2.19, 0.022)$
α^4	2.54	$(2.54, 0.036)$
α^5	2.49	$(2.49, 0.12)$
	Intrinsic alignments	
$A_{\rm IA}$	0.4	$[-5, 5\,]$
$\eta_{\rm IA}$	2.2	$[-5, 5\,]$
	Baryonic feedback	
$\log_{10}(T_{\rm AGN}/K)$	7.8	$[7.3, 8.3]$

and we also subtract the signal around random lenses. We performed measurements in 15 logarithmic angular separation bins in the range $0.3 < \theta < 300$ arcmin using the DSIGMA code[6] (Lange & Huang 2022), where we will later discuss in Sec. 3.5 the scale cuts we apply in model fits. Before performing the galaxy-galaxy lensing measurement, we cut the source and lens samples to overlapping sky areas (Heydenreich et al. 2025), whereas we use the full DESI sky coverage to perform the projected correlation function measurements described above.

3.3. *Parametrisation and priors*

We infer the cosmological parameters from the measured data vectors using Bayesian statistics, estimating the posterior probability distribution for the parameters $\mathbf{p}$ of the theoretical model M, given the data $\hat{\mathbf{D}}$, as

$$P(\mathbf{p}|\hat{\mathbf{D}}, M) \propto \mathcal{L}(\hat{\mathbf{D}}|\mathbf{p}, M)\, \Pi\,(\mathbf{p}|M)\,, \tag{17}$$

where $\Pi\,(\mathbf{p}|M)$ is the prior probability distribution for the parameters, and $\mathcal{L}(\hat{\mathbf{D}}|\mathbf{p}, M)$ is the likelihood of the data given a set of values for the parameters. We assume a Gaussian likelihood,

$$\ln \mathcal{L}(\hat{\mathbf{D}}|\mathbf{p}) = B - \frac{1}{2}\left(\hat{\mathbf{D}} - \mathbf{T}(\mathbf{p})\right)^{\rm T} \mathbf{C}^{-1} \left(\hat{\mathbf{D}} - \mathbf{T}(\mathbf{p})\right), \tag{18}$$

with a normalisation constant B, $T(\mathbf{p})$ being the vector of theoretical predictions for each correlation function included in the data vector $\hat{\mathbf{D}}$, calculated assuming a given set of parameters $\mathbf{p}$, and $\mathbf{C}$ being the covariance matrix of the data, described in Sec. 3.6. The proportionality constant of Eq. (17) is given by the inverse of the Bayesian evidence:

$$P(\hat{\mathbf{D}}|M) = \int \mathrm{d}\mathbf{p}\, \mathcal{L}(\hat{\mathbf{D}}|\mathbf{p})\, \Pi\,(\mathbf{p}|M)\,. \tag{19}$$

For some cases, we use the ratio of the Bayesian evidences to assess if the data prefer one model over the other (e.g. TATT over NLA). This approach has the advantage of penalising models with extra freedom in the parameter space. We use the Jeffreys scale (Jeffreys 1935) to interpret the evidence ratio results.

Table 1 lists the set of cosmological and astrophysical parameters, and their priors, considered in our analysis. We assume two main cosmological models, flat ΛCDM and flat wCDM with free neutrino mass[7]. Regarding cosmological parameters, we sample the total matter energy density $\Omega_{\rm m}$, the amplitude of primordial scalar density fluctuations $A_{\rm s}$, the spectral index $n_{\rm s}$ of the power spectrum, the energy density of baryons $\Omega_{\rm b}$, the Hubble parameter h, and the sum of neutrino masses $\Sigma\, m_\nu$. In wCDM, this list is extended to sample w, for the equation of state of dark energy, which is assumed to be constant with time. In ΛCDM this parameter is fixed to -1, the cosmological constant. In all cases, flatness is imposed by setting the dark energy density to $\Omega_\Lambda = 1 - \Omega_{\rm m}$. We follow DES Collaboration (2022) for the choice of prior ranges for these parameters. Although we sample the parameter $A_{\rm s}$, instead we report constraints on the rms amplitude of mass fluctuations on the $8\,h^{-1}\,\mathrm{Mpc}$ scale in linear theory, σ_8, or the related parameter $S_8 \equiv \sigma_8(\Omega_{\rm m}/0.3)^{0.5}$, which is typically constrained best by weak lensing analyses.

In addition to the cosmological parameters, we marginalise over several parameters related to the galaxy bias, lens magnification, intrinsic alignments, and baryonic feedback effects. As described in Sec. 3.1, we assume a linear galaxy bias model with one free amplitude parameter per redshift bin. For lens magnification, we also consider one amplitude parameter per redshift bin and assume Gaussian priors with mean and standard deviation from Table 3 of Heydenreich et al. (2025), where these coefficients were measured for our BGS and LRG lens redshift bins. The NLA modelling of intrinsic alignments consists of two free parameters, for which we assume wide flat priors following previous analyses (DES and KiDS Collaboration 2023; DES Collaboration 2022). In Sec. 4.3 we also consider the TATT IA model. In that case, we have five free nuisance parameters, for which we assume the same priors as NLA for A_1, η_1, A_2, and η_2, and the prior $[0, 2]$ for $b_{\rm TA}$ (following DES Collaboration 2022). Last, we model the impact of baryonic feedback effects, such as baryon cooling, star formation, and active galactic nuclei (AGN) feedback, on the non-linear matter power spectrum through the free parameter $T_{\rm AGN}$ of HMCODE2020, which has been calibrated with the BAHAMAS hydrodynamical simulations (McCarthy et al. 2017; van Daalen et al. 2020). $T_{\rm AGN}$ maps to the BAHAMAS-defined heating temperature of the AGN, modulating the strength of the baryon feedback suppression of the matter power spectrum. We adopt a top-hat prior on $\log_{10}(T_{\rm AGN}/K)$ of $[7.3, 8.3]$, where the lower limit follows DES and KiDS Collaboration (2023), and the upper limit is increased following McCullough et al. (2024) to account for the recent evidence of stronger baryonic-feedback suppression (see, e.g., Hadzhiyska et al. 2023; Bigwood et al. 2024).

Table 2 lists the data-calibration nuisance parameters and their priors as provided by each weak lensing survey: DES-Y3 (Amon et al. 2022; Secco, Samuroff et al. 2022), KiDS-1000 (Asgari et al. 2021), and HSC-Y3 (Li et al. 2023). With these, we marginalise over the uncertainties related to photometric redshifts, shear calibration and, in the case of HSC,

[6] https://dsigma.readthedocs.io/

[7] We consider a variation with fixed neutrino mass in Sec. 4.3.

Table 2. Priors for the nuisance parameters related to the calibration of the weak-lensing data from DES-Y3, KiDS-1000, and HSC-Y3. Square brackets denote a flat prior, while parentheses denote a Gaussian prior of the form $\mathcal{N}(\mu, \sigma)$. The Gaussian priors are, in general, uncorrelated between tomographic bins, except for the KiDS-1000 parameters related to shear m^j and photometric redshift uncertainties Δz^j. In that case, the priors are correlated and modelled through a five-dimensional multivariate Gaussian prior with mean $\boldsymbol{\mu}$ and covariance $\boldsymbol{C}$. We list the diagonal of the covariance as $\sigma^j = \sqrt{C^{jj}}$, and denote these correlated priors as $(\mu^j, \sigma^j)_{\rm c}$.

Parameter	DES-Y3	KiDS-1000	HSC-Y3
		Photometric redshifts	
Δz^1	$(0.0, 0.018)$	$(0.000, 0.011)_{\rm c}$	$(0.0, 0.024)$
Δz^2	$(0.0, 0.015)$	$(0.002, 0.011)_{\rm c}$	$(0.0, 0.022)$
Δz^3	$(0.0, 0.011)$	$(0.013, 0.012)_{\rm c}$	$[-1.0, 1.0]$
Δz^4	$(0.0, 0.017)$	$(0.011, 0.009)_{\rm c}$	$[-1.0, 1.0]$
Δz^5	-	$(-0.006, 0.010)_{\rm c}$	-
		Shear calibration	
m^1	$(-0.0063, 0.0091)$	$(-0.009, 0.019)_{\rm c}$	$(0.00, 0.01)$
m^2	$(-0.0198, 0.0078)$	$(-0.011, 0.020)_{\rm c}$	$(0.00, 0.01)$
m^3	$(-0.0241, 0.0076)$	$(-0.015, 0.017)_{\rm c}$	$(0.00, 0.01)$
m^4	$(-0.0369, 0.0076)$	$(0.002, 0.012)_{\rm c}$	$(0.00, 0.01)$
m^5	-	$(0.007, 0.010)_{\rm c}$	-
$\delta_{\rm c} \times 10^4$	-	$(0.0, 2.3)$	-
		PSF systematics	
$\alpha^{(2)}_{\rm PSF}$	-	-	$(0.0, 1.0)$
$\beta^{(2)}_{\rm PSF}$	-	-	$(0.0, 1.0)$
$\alpha^{(4)}_{\rm PSF}$	-	-	$(0.0, 1.0)$
$\beta^{(4)}_{\rm PSF}$	-	-	$(0.0, 1.0)$

systematics associated with the modelling of the point-spread function (PSF).

Photometric redshifts — We parametrise photometric redshift uncertainties via an additive shift to the mean redshift of each source tomographic bin j, given by Δz^j such that,

$$n^j(z) \to n^j(z - \Delta z^j). \tag{20}$$

While DES-Y3 and HSC-Y3 assume these parameters to be independent, KiDS-1000 takes into account the correlated uncertainty between bins via a multivariate Gaussian prior. See Sec. 3.3 of Joachimi et al. (2021) for details.

Shear calibration — The uncertainty associated with the shear estimation is typically parametrised by the shear calibration bias parameters m^j, which relate the measured ellipticity of galaxies to the true shear. In terms of two-point correlation functions, we have

$$\xi^{ij}_{\pm}(\theta) \to (1 + m^i)(1 + m^j)\, \xi^{ij}_{\pm}(\theta). \tag{21}$$

We assume Gaussian priors for these parameters, as validated and provided by each weak lensing survey. In the case of KiDS-1000, these parameters are assumed to be 100% correlated between bins. The correlated uncertainty is then included in the analytical covariance for the cosmic shear data vector (see Eq. (37) in Joachimi et al. 2021). Additionally, when using ξ_+, KiDS-1000 considers an additive shear bias term, such that $\xi_+ \to \xi_+ + \delta_c^2$.

PSF systematics — HSC-Y3 additionally marginalises over four PSF-related nuisance parameters. $\alpha^{(2)}_{\rm PSF}$ and $\alpha^{(4)}_{\rm PSF}$ correspond to the PSF leakage bias by the 2nd and 4th moments of the PSF shapes, while $\beta^{(2)}_{\rm PSF}$ and $\beta^{(4)}_{\rm PSF}$ are related to the PSF modelling error in the 2nd and 4th-order moments. See Eqs. (24-28) in Li et al. (2023) for the full expression of these terms. Given that Zhang et al. (2023) found the bias on ξ_- due to PSF systematics to be negligible, this uncertainty is only accounted for ξ_+. Following Li et al. (2023), we take into account the correlation between these four parameters in the likelihood inference.

We use the COSMOSIS framework for the modelling and likelihood evaluation, and its implementation of NAUTILUS[8] (Lange 2023) to sample the posterior probability distribution of the parameters and estimate the Bayesian evidence. The configuration we use for NAUTILUS consists of $n_{\rm live} = 10000$ for the number of live points, $n_{\rm networks} = 16$ for the number of neural networks used in the estimator, and the discard-exploration mode (so-called "nautilus-r" in Lange 2023). We then analyse these samples with the GETDIST[9] package (Lewis 2025) to visualise the one- and two-dimensional posterior probability distributions of the parameters.

When reporting parameter constraints in Sec. 4, we provide the mean of the 1D marginalised posterior distribution, along with a credible interval that encompasses 68% of the marginal posterior density around the mean of the distribution. We use the COSMOSIS `postprocess` function to obtain these statistics. We also provide, in parentheses, the *Maximum a Posteriori* (MAP) values for each constraint. To estimate these with high accuracy, we iteratively run the MAX-LIKE sampler from COSMOSIS five times, starting with the maximum posterior value of the NAUTILUS CHAIN. We use the `Powell` method with a tolerance of 0.05 and a maximum of 1000 iterations.

3.4. *Quantifying consistency and goodness of fit*

We use the weighted least squares (χ^2) statistic evaluated at the best-fit parameters, $\chi^2_{\rm min}$, to assess the goodness of fit of the model to the data points. We can then quantify the goodness of fit with $p(\chi^2 > \chi^2_{\rm min} | \, \nu_{\rm eff})$, which is the probability that a χ^2 exceeds $\chi^2_{\rm min}$, assuming that it follows a χ^2 distribution with an effective number of degrees of freedom $\nu_{\rm eff} = N_{\rm D} - N_{\rm p,eff}$. Here, $N_{\rm D}$ is the total number of data points, and $N_{\rm p,eff}$ is the effective number of free parameters, which is typically smaller than the total number of free parameters due to the use of informative priors and existing correlations between parameters.

To estimate the effective number of free parameters, we follow Eq. (29) of Raveri & Hu (2019),

$$N_{\rm p,eff} \equiv N_{\rm p} - {\rm tr}[\mathbf{C}_\Pi^{-1} \mathbf{C}_P], \tag{22}$$

where $N_{\rm p}$ is the total number of free parameters that are sampled, $\mathbf{C}_\Pi$ is the covariance of the prior probability distribution, and $\mathbf{C}_P$ is the covariance of the posterior distribution. We use COSMOSIS to sample the prior distribution and the TENSIOMETER[10] package to estimate $N_{\rm p,eff}$ from Eq. (22).

To assess the consistency between two different analyses and, given that the posterior distributions might be non-Gaussian, we use the non-Gaussian estimates of parameter shifts provided by the TENSIOMETER package. In particular, we use the kernel density estimator algorithm from Raveri & Doux (2021) to estimate the probability distribution of parameter shifts $P(\boldsymbol{\Delta\theta})$ and quantify the posterior mass above the

[8] https://nautilus-sampler.readthedocs.io/
[9] https://getdist.readthedocs.io/
[10] https://tensiometer.readthedocs.io

iso-contour of "*no shift*" ($\boldsymbol{\Delta}\theta = 0$),

$$\Delta = \int_{P(\boldsymbol{\Delta}\theta)>P(\mathbf{0})} \mathrm{d}\boldsymbol{\Delta}\theta \, P(\boldsymbol{\Delta}\theta). \tag{23}$$

We then convert this probability into an effective number of standard deviations σ through $n_{\sigma,\mathrm{eff}}(P) = \sqrt{2}\,\mathrm{Erf}^{-1}(\mathrm{P})$, following Raveri & Hu (2019). We have compared these estimates with those from the Gaussian estimator $Q_{\rm DM}$, defined in Raveri & Hu (2019), finding practically the same statistical significance for the main cosmological parameters of interest, $\Omega_{\rm m}$ and S_8.

3.5. *Scale cuts*

In an accompanying paper (Emas et al. 2026), we validate our modelling and scale cut choices for the fits to the data (for either cosmic shear, the combination of projected galaxy clustering and galaxy-galaxy lensing, or 2×2-pt, and the full 3×2-pt analysis). Starting from the fiducial scale cuts for cosmic shear from each survey, we follow the methodology of Krause et al. (2021) to ensure that our modelling is robust (in the scales included) against uncertainties in the modelling of the non-linear matter power spectrum and non-linear galaxy bias. We therefore remove the smallest scales from our analysis, to mitigate the sensitivity to these modelling uncertainties.

The methodology consists of comparing the cosmology contours between synthetic data vectors generated with either our *"baseline"* model or a *"contaminated"* model that includes an additional or alternative effect not included in our baseline choice. To ensure robustness against a given "contamination" or modelling choice, we set a threshold of $\leq 0.3\sigma$ in the $S_8 - \Omega_{\rm m}$ 2D plane (and $w - \Omega_{\rm m}$ for wCDM) for the difference between the baseline and contaminated posterior distributions. The "contaminating" effects we consider are non-linear galaxy bias, baryonic feedback effects imprinted in the matter power spectrum, and an alternative non-linear matter power spectrum prediction. To generate these synthetic data vectors, we rely on the hybrid effective field theory (HEFT) (Modi et al. 2020) implementation of the AEMULUS ν emulator from DeRose et al. (2023), which has been used in a previous 2×2-pt analysis of DESI-DR1 and DES-Y3 data (Chen et al. 2024).

After testing against these modelling effects for all probe and survey combinations, we find that the fiducial scale cuts for DES-Y3 (Amon et al. 2022; Secco, Samuroff et al. 2022) and for HSC-Y3 (Li et al. 2023) cosmic shear are still valid for our analysis. For KiDS-1000 cosmic shear, however, we find that the fiducial scales from Asgari et al. (2021) marginally do not satisfy our threshold criteria. In this case, we follow the methodology from Krause et al. (2021) for cosmic shear to decide which data points to remove first from the analysis, based on the χ^2 difference between baseline and contaminated predictions for each pair-bin combination $\xi_{\pm}^{ij}$. We found that we could meet our 0.3σ threshold criteria by changing the ξ_- scale cuts from $4'$ to $6.06'$, which just removes one additional data point in some bin combinations with respect to Asgari et al. (2021). The fiducial scale cuts for ξ_+ ($0.5'$) remain unchanged.

The scale cuts for galaxy-galaxy lensing and projected galaxy clustering are defined in terms of the projected separation $r_{\rm p}$, which we convert to angular scales for $\gamma_{\rm t}$ using $\theta^i_{\rm min} = r_{\rm p,min}/\chi(z^i_{\rm lens})$, with $\chi(z^i_{\rm lens})$ being the value of the comoving distance at the effective redshift of lens bin i. We find that the scale cuts $(r_{\rm p,ggl},\, r_{\rm p,clus}) = (6,\, 8)\, h^{-1}\,$Mpc for galaxy-galaxy lensing and galaxy clustering, respectively, satisfy our validation criteria for all combinations. We note that these scales correspond to those used in the DES-Y3 analysis for the linear galaxy bias model (Krause et al. 2021; Porredon et al. 2022; DES Collaboration 2022).

3.6. *Covariance*

We now summarise the covariance model we adopt for our set of 3×2-pt correlation functions $\{\xi_{\pm}(\theta), \gamma_t(\theta), w_p(r_p)\}$. The foundation of our model is a Gaussian analytical covariance including sample variance, noise and mixed terms. Our implementation of these terms for the auto- and cross-covariances of the different 2-pt correlations, between different source and lens samples, is fully presented in Appendices A-D of Blake et al. (2025); our computations follow frameworks previously presented by Krause & Eifler (2017) and Joachimi et al. (2021). For the cosmic shear covariance we include super-sample variance (Takada & Hu 2013), and we also apply a small-scale noise correction to all covariances based on the number of observed pairs within the survey geometry (Troxel et al. 2018). We corrected the galaxy-galaxy lensing covariance for footprint boundary effects using an ensemble of fast mocks sampled to the angular selection function of the lensing surveys, as discussed by Yuan et al. (2024).

We validated our analytical covariance pipeline through comparison with three existing codes: COSMOCOV (Krause & Eifler 2017; Fang et al. 2020b) used by DES, the code used by KiDS-1000 (Joachimi et al. 2021), and the ONECOVARIANCE framework (Reischke et al. 2025) employed by the KiDS-Legacy analysis (these first two validations are discussed in Appendix E of Blake et al. 2025). We specifically used ONECOVARIANCE to validate that the non-Gaussian contribution to the cosmic shear and galaxy-galaxy lensing covariance was negligible for our configurations (i.e., had no significant effect on χ^2 values). We also ran test cosmology fits in which we replaced our fiducial cosmic shear covariance with the equivalent versions generated by the DES-Y3, KiDS-1000 and HSC-Y3 collaborations (Friedrich et al. 2021; Joachimi et al. 2021; Li et al. 2023), validating that our cosmological results in these cases were not significantly changed. For the final cosmology results from Sec. 4 we use a jack-knife covariance for $w_{\rm p}$, estimated in Heydenreich et al. (2025), instead of the analytical prediction. This change does not impact the final cosmological constraints, but it significantly improves the goodness-of-fit statistics, as discussed in Sec. 4. The reason for this is that the analytical covariance estimate for $w_{\rm p}$ does not currently include the footprint boundary effects.

Our shear and clustering datasets cover different sky areas, which only partially overlap. We corrected our covariance model for this effect by assuming that correlation measurements in non-overlapping regions are uncorrelated (which was found to be a safe assumption by DES and KiDS Collaboration 2023). If the sky area coverage of two datasets is Ω_1 and Ω_2, with overlap area Ω_O, then the covariance of the correlation functions of these datasets should be scaled by $\Omega_O^2/\Omega_1\Omega_2$ in comparison with fully-overlapping measurements (Blake et al. 2025). The full set of areas assumed in our covariance model is reproduced in Table 3.

3.7. *Blinding*

We implement a blinding procedure to safeguard our analysis against cognitive biases such as confirmation bias. To this

Table 3. The areas of the DESI-DR1 and weak lensing surveys used in our covariance model, and their intersections, in square degrees. The row and column labelled "Full" provide the area of the individual components, and the remainder of the table quotes the areas of intersection. The DESI sample is divided into BGS, LRG, and the common area (BGS+LRG). The "Full" areas for the lensing surveys are quoted from the survey collaborations, and the remaining areas are evaluated on an $n_{\rm side} = 1024$ HEALPIX grid.

WL survey	Full	DESI-BGS	DESI-LRG	DESI-BGS+LRG
Full	–	9146.5	8607.6	6285.5
DES-Y3	4143.0	716.8	851.2	587.5
KiDS-1000	773.3	448.2	446.8	446.3
HSC-Y1	136.9	142.1	151.8	139.0
HSC-Y3	417.0	440.6	440.5	413.3

end, the goal of our blinding procedure is to randomly shift cosmological parameter constraints in our analysis. This allows us to perform a variety of robustness tests without potentially being influenced by expectations about what our analysis should reveal in terms of cosmology. Only after passing the robustness test do we run the analysis on unblinded data and obtain our actual cosmological constraints.

Our blinding procedure is based on altering the data vectors, i.e., the 3×2-pt correlation functions $\xi_{\rm D} = \{\xi_\pm, \gamma_{\rm t}, w_{\rm p}\}$. Given a random set of shifts in the cosmological parameters, $\Delta\mathcal{C}$, the blinding method produces a new blinded data vector $\tilde{\xi}_{\rm D} = \xi_{\rm D} + \Delta\xi$ whose posterior is roughly shifted by $\Delta\mathcal{C}$ with respect to that of $\xi_{\rm D}$. At the same time, the blinded data vector $\tilde{\xi}_{\rm D}$ should be equally sensitive to robustness tests, e.g., should result in a similar χ^2 with respect to the best-fit model $\tilde{\xi}_{\rm T}$. Muir et al. (2020) introduced the following blinding function,

$$\Delta\xi = \xi_{\rm T}(\mathcal{C}_{\rm bli}, \mathcal{N}_{\rm fid}) - \xi_{\rm T}(\mathcal{C}_{\rm fid}, \mathcal{N}_{\rm fid})\,. \quad (24)$$

In the above equation, $\mathcal{C}_{\rm fid}$ represents a choice of fiducial cosmological parameters, $\mathcal{C}_{\rm bli} = \mathcal{C}_{\rm fid} + \Delta\mathcal{C}$ and $\mathcal{N}_{\rm fid}$ are fiducial nuisance parameters such as galaxy bias parameters. Muir et al. (2020) showed that, when applied to the DES-Y3 analysis, this simple procedure shifts the cosmological posterior of $\tilde{\xi}_{\rm D}$ by roughly $\Delta\mathcal{C}$ while leaving the goodness of fit largely unchanged. In this work, we implement a slightly modified version of that blinding approach:

$$\Delta\xi = \xi_{\rm T}(\mathcal{C}_{\rm bli}, \mathcal{N}(\mathcal{C}_{\rm bli})) - \xi_{\rm T}(\mathcal{C}_{\rm fid}, \mathcal{N}(\mathcal{C}_{\rm fid}))\,. \quad (25)$$

In the above equation, compared to Muir et al. (2020), we do not choose a fiducial set of nuisance parameters but instead optimise them with respect to the cosmological parameters. In particular, the nuisance parameters $\mathcal{N}(\mathcal{C})$ are chosen so that they minimise the squared Mahalanobis distance, i.e., the χ^2, between the data, $\xi_{\rm D}$, and the model, $\xi_{\rm T}$ for a fixed cosmology $\mathcal{C}$. The motivation for this slightly different procedure is that it minimises an upper bound on the shift $\Delta\xi$, i.e.,

$$\begin{aligned}\|\Delta\xi\|^2 \leq & 2\|\xi_{\rm T}(\mathcal{C}_{\rm bli}, \mathcal{N}(\mathcal{C}_{\rm bli})) - \xi_{\rm D}\|^2 + \\ & 2\|\xi_{\rm T}(\mathcal{C}_{\rm fid}, \mathcal{N}(\mathcal{C}_{\rm fid})) - \xi_{\rm D}\|^2\,.\end{aligned} \quad (26)$$

In other words, the data vector shift $\Delta\xi$ is guaranteed to be small since both theory data vectors are similar to the observed data vector. In practice, in this work, we only blind the cosmological parameters $\Omega_{\rm m}$ and σ_8 and only optimise the galaxy bias parameters when it comes to nuisance parameters. All other cosmological and nuisance parameters are left at their fiducial choice. In particular, we choose $\Omega_{\rm m,fid} = 0.3166$ and $\sigma_{8,\rm fid} = 0.8120$ and draw $\Delta\Omega_{\rm m}$ and $\Delta\sigma_8$ from uniform distributions with ranges $[-0.05, +0.05]$ and $[-0.12, +0.12]$, respectively. We tested that this procedure works reliably on mock data, i.e., produces shifts in line with the expected shift $\Delta\mathcal{C}$ while not leading to significant shifts in the best-fit χ^2.

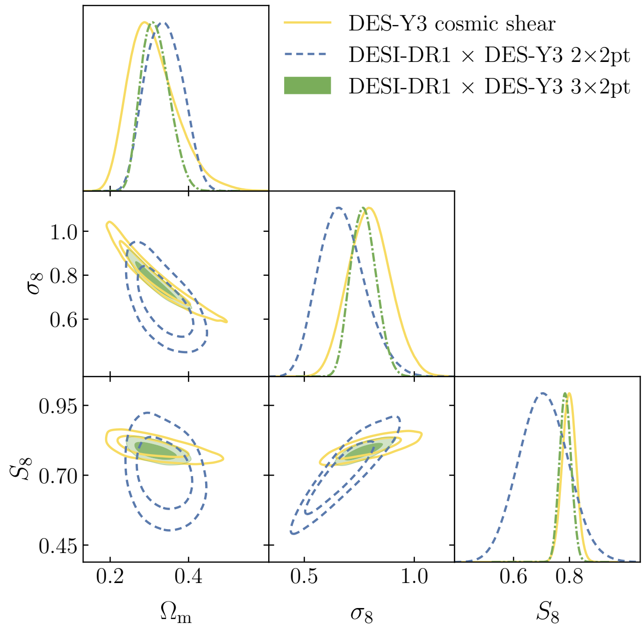

Figure 1. Marginalised constraints on $\Omega_{\rm m}$, σ_8, and S_8 in ΛCDM for DES-Y3 cosmic shear (solid yellow), the combination of galaxy-galaxy lensing and projected galaxy clustering from DESI-DR1 (dashed blue), and the 3×2-pt combination (solid green).

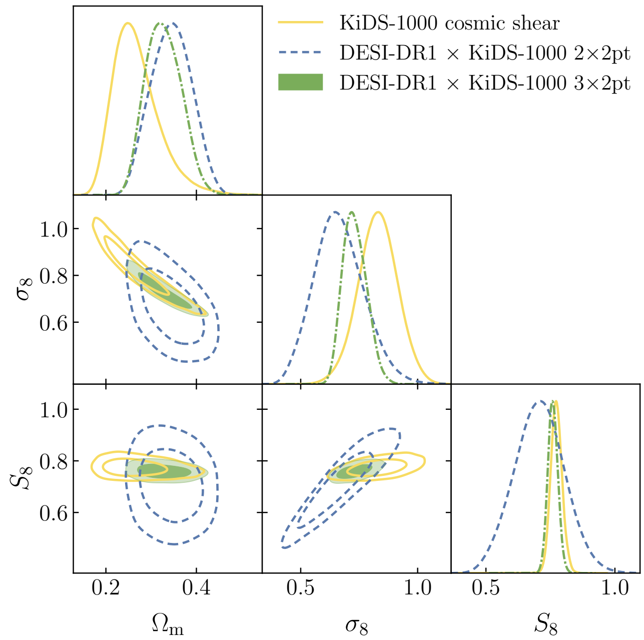

Figure 2. Marginalised constraints on $\Omega_{\rm m}$, σ_8, and S_8 in ΛCDM for KiDS-1000 cosmic shear (solid yellow), the combination of galaxy-galaxy lensing and projected galaxy clustering from DESI-DR1 (dashed blue), and the 3×2-pt combination (solid green).

4. COSMOLOGICAL RESULTS

In this section, we provide cosmological results for the ΛCDM (Sec. 4.1) and wCDM models (Sec. 4.2) for each weak lensing survey and probe combination. In Sec. 4.3, we

Table 4. Constraints on S_8, Ω_m, and σ_8 in ΛCDM with 68% credible intervals using the mean 1D marginal posterior distribution. For each weak lensing dataset, we report constraints on cosmic shear, the combination of DESI-DR1 projected galaxy clustering and galaxy-galaxy lensing ($2\times$ 2-pt), and the full $3\times$ 2-pt data vector. Along with the marginalised constraints, we provide goodness of fit statistics: the χ^2 value at the best fit ($\chi^2_{\rm min}$), the total number of data points $N_{\rm D}$, the estimated effective number of free parameters $N_{\rm p,eff}$, the reduced $\chi^2_{\rm red}=\chi^2_{\rm min}/(N_{\rm D}-N_{\rm p,eff})$, and the goodness of fit probability p (see Sec. 3.4 for more details).

Analysis	S_8	Ω_m	σ_8	$\chi^2_{\rm min}$	$N_{\rm D}$	$N_{\rm p,eff}$	$\chi^2_{\rm red}$	$p(\chi^2_{\rm red})$
DES-Y3								
Cosmic shear	$0.799^{+0.025}_{-0.025}$	$0.311^{+0.074}_{-0.043}$	$0.797^{+0.104}_{-0.090}$	241.72	227	4.41	1.09	0.18
$2\times$ 2-pt	$0.707^{+0.090}_{-0.086}$	$0.337^{+0.049}_{-0.046}$	$0.673^{+0.115}_{-0.089}$	131.55	137	8.86	1.03	0.40
$3\times$ 2-pt	$0.786^{+0.022}_{-0.019}$	$0.316^{+0.040}_{-0.031}$	$0.770^{+0.062}_{-0.054}$	396.02	364	10.19	1.12	0.06
KiDS-1000								
Cosmic shear	$0.773^{+0.023}_{-0.020}$	$0.268^{+0.060}_{-0.032}$	$0.830^{+0.081}_{-0.082}$	237.22	221	3.90	1.09	0.17
$2\times$ 2-pt	$0.707^{+0.094}_{-0.098}$	$0.345^{+0.046}_{-0.046}$	$0.665^{+0.116}_{-0.096}$	163.47	165	8.61	1.05	0.33
$3\times$ 2-pt	$0.760^{+0.020}_{-0.018}$	$0.327^{+0.043}_{-0.036}$	$0.731^{+0.059}_{-0.045}$	414.84	386	9.80	1.10	0.08
HSC-Y3								
Cosmic shear	$0.775^{+0.031}_{-0.032}$	$0.313^{+0.072}_{-0.044}$	$0.770^{+0.094}_{-0.091}$	141.63	140	6.47	1.06	0.30
$2\times$ 2-pt	$0.649^{+0.091}_{-0.067}$	$0.347^{+0.046}_{-0.048}$	$0.609^{+0.110}_{-0.072}$	99.71	137	11.34	0.79	0.55
$3\times$ 2-pt	$0.771^{+0.026}_{-0.027}$	$0.355^{+0.040}_{-0.040}$	$0.712^{+0.060}_{-0.042}$	246.56	277	12.85	0.93	0.77

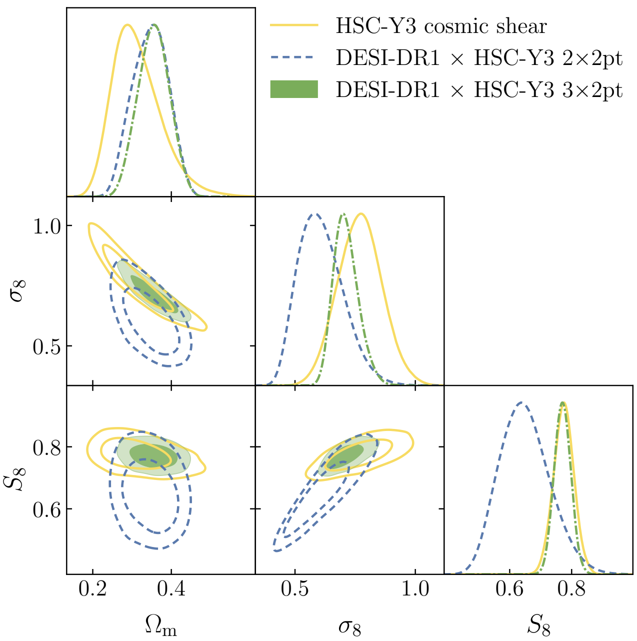

Figure 3. Marginalised constraints on Ω_m, σ_8, and S_8 in ΛCDM for HSC-Y3 cosmic shear (solid yellow), the combination of galaxy-galaxy lensing and projected galaxy clustering from DESI-DR1 (dashed blue), and the $3\times$2-pt combination (solid green).

then carry out several analysis variations to assess the robustness of our main results.

We first analysed the blinded data vectors from Sec. 3.7 and ensured that: (1) the best-fit goodness of fit χ^2 has $p > 0.01$ for each of the results (including combinations such as $\xi_\pm + w_p$ and $\xi_\pm + \gamma_t$, to identify potential issues with individual observables), (2) the posteriors of nuisance parameters with Gaussian priors from Table 2 are not hitting the edges of the priors, and (3) the cosmic shear and $2\times$ 2-pt constraints for each WL survey are internally consistent (see Sec. 3.4 for details).

Our first blinded results provided low goodness-of-fit p values for most cases. After comparison with the fiducial covariances from the cosmic shear analyses, we corrected the covariances for cosmic shear and galaxy-galaxy lensing by accounting for the exact number of pairs (Troxel et al. 2018) (see Sec. 3.6). After this correction, we still found low p values when including w_p in the likelihood inference, which was resolved after replacing the w_p analytical covariance, which is the least accurate of the observables due to footprint effects, with the jack-knife covariance estimated in Heydenreich et al. (2025). After these changes, we still found low goodness-of-fit p values for some combinations using HSC Year 1 data. We report cosmological constraints with HSC-Y1 in Appendix A for completeness. We note that the changes to the covariance did not significantly affect the resulting fitted parameter values.

4.1. ΛCDM

We have obtained cosmological constraints using projected galaxy clustering from DESI-DR1 and weak lensing data from DES-Y3, KiDS-1000, and HSC-Y3. We show the marginalised posterior distributions for the main constrained cosmological parameters, Ω_m, S_8, and σ_8, in Figs. 1, 2, and 3. In Table 4, we report the 68% credible intervals around the mean 1D marginal posterior distribution for these parameters, along with the goodness of fit metrics for each case. Our best constrained parameter is S_8 when using the whole $3\times$ 2-pt data vector:

$$\begin{aligned}
\text{DESI-DR1} \times \text{DES-Y3}: &\quad S_8 = 0.786^{+0.022}_{-0.019}\ (0.790),\\
\text{DESI-DR1} \times \text{KiDS-1000}: &\quad S_8 = 0.760^{+0.020}_{-0.018}\ (0.776),\\
\text{DESI-DR1} \times \text{HSC-Y3}: &\quad S_8 = 0.771^{+0.026}_{-0.027}\ (0.763),
\end{aligned}$$

corresponding to 2.6% (DES-Y3), 2.5% (KiDS-1000), and 3.4% (HSC-Y3) precision measurements.

We provide additional posterior distributions for the $3\times$ 2-pt analyses in Appendix B. Besides the main cosmological parameters, with DES-Y3 and KiDS-1000 data, we are able to constrain the amplitude of intrinsic alignments under our fiducial NLA model,

$$\begin{aligned}
\text{DESI-DR1} \times \text{DES-Y3}: &\quad A_{\rm IA} = 0.36^{+0.49}_{-0.27}\ (0.43),\\
\text{DESI-DR1} \times \text{KiDS-1000}: &\quad A_{\rm IA} = 0.55^{+0.54}_{-0.28}\ (0.08),
\end{aligned}$$

finding values very consistent with the constraints obtained for these cosmic shear data sets in DES and KiDS Collabo-

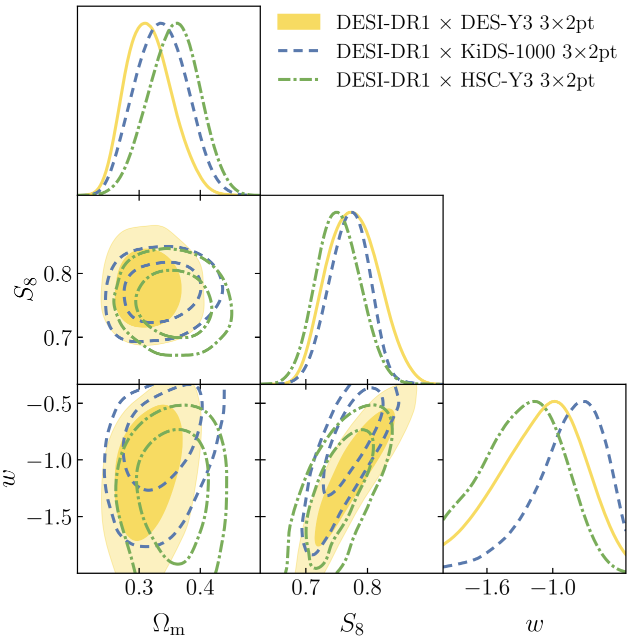

Figure 4. Marginalised constraints on Ω_m, S_8, and w in wCDM from the 3×2-pt combination of DESI-DR1 projected galaxy clustering and weak lensing data from DES-Y3 (solid yellow), KiDS-1000 (dashed blue), and HSC-Y3 (dash-dotted green).

ration (2023). In the case of HSC-Y3, we find unconstrained posteriors for the intrinsic alignment parameters that hit the edges of the priors, probably due to the fact that the data have to self-calibrate the photometric redshift parameters in source bins 3 and 4, for which we assume wide flat priors (see Table 2). For these Δ_z parameters, we obtain:

$$\text{DESI-DR1} \times \text{HSC-Y3}: \quad \Delta_z^3 = 0.068^{+0.041}_{-0.039}\ (0.071),$$
$$\text{DESI-DR1} \times \text{HSC-Y3}: \quad \Delta_z^4 = 0.166^{+0.071}_{-0.069}\ (0.179).$$

These constraints are consistent within 1σ with the results reported by the HSC Y3 fiducial analyses (Li et al. 2023; Dalal et al. 2023)[11], but tighter by 27% and 20%, respectively, thanks to the use of DESI-DR1 data as lenses in this 3×2-pt analysis. Since then, other works in the literature have obtained constraints on these parameters (Rana et al. 2026, Zhang et al. 2025, and Choppin de Janvry et al. 2025a,b), which are in general consistent with our constrains at the 1σ level, with the exception of the Δ_z^4 constraint from Choppin de Janvry et al. (2025a), which is consistent within 2σ. We note that Choppin de Janvry et al. (2025a) has done an independent calibration of the HSC Y3 redshift distributions, with additional DESI data that is not considered in this work. Here, we just give freedom to these parameters to self-calibrate, obtaining posterior distributions that are correlated between redshift bins and with the intrinsic alignment parameters (see Fig. 14). As a result, there could be shifts along the degeneracy directions for poorly constrained parameters in the analysis. In any case, all these constraints are well within the priors assumed in our analysis, so we do not expect a significant change in our results from the different Δ_z values in bins 3 and 4.

[11] Note that the sign convention for Δ_z we assume in Eq. (20) is different to what is assumed in the official HSC Y3 analysis. A positive value here corresponds to a negative value in Li et al. (2023).

4.2. *wCDM*

We now use our most constraining data combination, 3×2-pt, to constrain the equation of state of dark energy, w, within the wCDM model. Fig. 4 shows the marginalised posterior distributions of w, Ω_m, and S_8 for each survey combination. Similarly to the ΛCDM case, we provide the 68% credible intervals around the 1D mean marginal in Table 5, including the constraints for σ_8 and the goodness-of-fit metrics. We find that the constraints are consistent between surveys and with the ΛCDM expectation of $w = -1$,

$$\text{DESI-DR1} \times \text{DES-Y3}: \quad w = -1.12^{+0.32}_{-0.45}\ (-0.96),$$
$$\text{DESI-DR1} \times \text{KiDS-1000}: \quad w = -0.88^{+0.18}_{-0.42}\ (-0.87),$$
$$\text{DESI-DR1} \times \text{HSC-Y3}: \quad w = -1.27^{+0.33}_{-0.40}\ (-1.31).$$

4.3. *Robustness tests*

In this section, we assess the robustness and internal consistency of our main results, i.e. the 3×2-pt cosmological constraints in ΛCDM for each survey combination. We first re-analyse the data, removing one lens bin at a time, to test its internal consistency. In addition, we consider alternative modelling choices such as fixing the sum of the neutrino masses, using the TATT model for intrinsic alignments, and using the HMCODE2020 matter power spectrum without the impact of baryonic feedback effects (dark-matter only). The 1D marginalised constraints for each of these cases are shown in Fig. 5.

Fig. 5 demonstrates that our main results from 3×2-pt are robust to variations of the lens redshift bin and alternative modelling choices, with most of the shifts being much smaller than 1σ. The largest shift corresponds to using the TATT model for intrinsic alignments, which shifts the S_8 constraint to lower values. This tendency has been observed in other analyses when switching from NLA to TATT (see, e.g., Amon et al. 2022, Secco, Samuroff et al. 2022, DES and KiDS Collaboration 2023, and Anbajagane et al. 2025b) and is attributed to the extra freedom allowed by the TATT model, which enables lower S_8 values for some values of the TATT parameters. To assess whether the data prefers the TATT or the NLA model, we compute the ratio of Bayesian evidences for each survey combination. In Table 6 we provide the S_8 constraints when assuming the TATT model along with the Bayesian ratio R of TATT to NLA and goodness-of-fit statistics. The ratio values indicate that TATT is disfavoured in the 3×2-pt analyses with DES-Y3 and HSC-Y3 data, but favoured in the case of KiDS-1000. Fig. 11 shows that the DESI-DR1 × KiDS-1000 analysis is able to additionally constrain the A_2 and η_2 parameters, with $A_2 = -1.83^{+0.57}_{-0.58}$, which explains the preference for the TATT model in this case (with A_2 being away from 0). The MAP estimate for S_8 in this case is 0.735, very similar to the mean of the posterior, indicating that the KiDS-1000 S_8 constraint with TATT is not impacted by prior volume effects[12]. Regarding goodness-of-fit metrics, we find very similar p-values when using TATT for the 3×2-pt combinations with DES-Y3 and HSC-Y3 compared to the fiducial values with NLA from Table 4. In the case of KiDS-1000, we do find an improvement in the

[12] This is not the case for DES-Y3, in which we find a $\sim 1\sigma$ difference between the mean and the MAP estimates. This shift could be due to prior volume effects from the extra unconstrained parameters η_1, η_2 and b_{TA} (see Fig. 11).

Table 5. Constraints on S_8, $\Omega_{\rm m}$, and σ_8 in wCDM with 68% credible intervals using the mean 1D marginal posterior distribution. For each weak lensing dataset, we report constraints on the 3×2-pt combination with DESI-DR1 projected galaxy clustering. Along with the marginalised constraints, we provide goodness of fit statistics: the χ^2 value at the best fit ($\chi^2_{\rm min}$), the total number of data points $N_{\rm D}$, the estimated effective number of free parameters $N_{\rm p,eff}$, the reduced $\chi^2_{\rm red} = \chi^2_{\rm min}/(N_{\rm D} - N_{\rm p,eff})$, and the goodness of fit probability p (see Sec. 3.4 for more details).

WL survey	S_8	$\Omega_{\rm m}$	σ_8	w	$\chi^2_{\rm min}$	$N_{\rm D}$	$N_{\rm p,eff}$	$\chi^2_{\rm red}$	$p(\chi^2_{\rm red})$
DES-Y3	$0.777^{+0.045}_{-0.039}$	$0.316^{+0.043}_{-0.032}$	$0.760^{+0.064}_{-0.057}$	$-1.12^{+0.32}_{-0.45}$	395.87	364	10.26	1.12	0.06
KiDS-1000	$0.770^{+0.030}_{-0.035}$	$0.336^{+0.043}_{-0.043}$	$0.732^{+0.057}_{-0.045}$	$-0.88^{+0.18}_{-0.42}$	413.50	386	10.04	1.10	0.09
HSC-Y3	$0.753^{+0.036}_{-0.034}$	$0.357^{+0.038}_{-0.044}$	$0.694^{+0.063}_{-0.045}$	$-1.27^{+0.33}_{-0.40}$	246.52	277	13.18	0.93	0.77

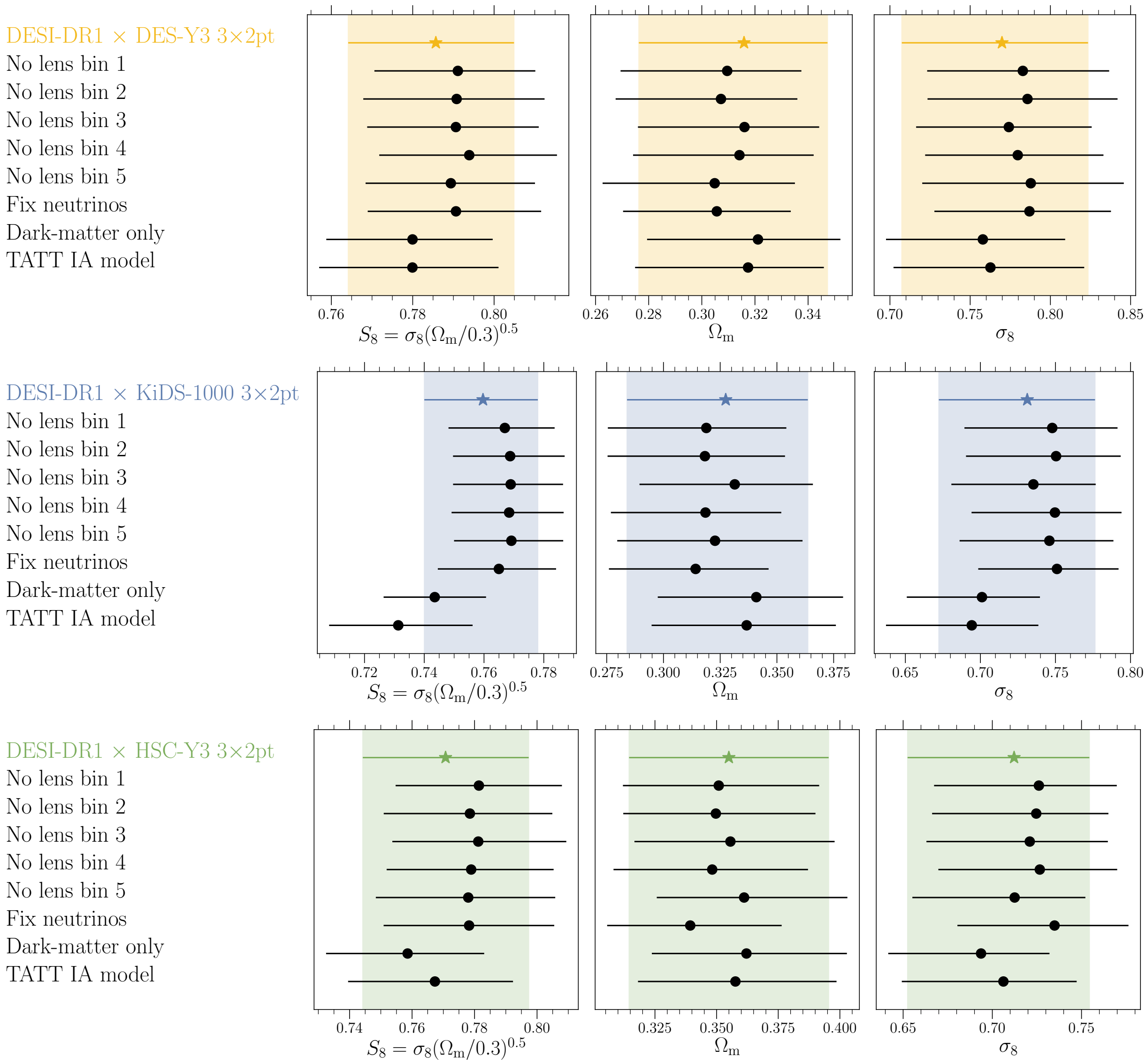

Figure 5. Comparison of 68% C.I. constraints on S_8, $\Omega_{\rm m}$, and σ_8, in ΛCDM from the 3×2-pt combination of DESI-DR1 projected galaxy clustering and weak lensing data from DES-Y3, KiDS-1000, and HSC-Y3 for several variation of analysis choices.

goodness-of-fit when using TATT, with $p = 0.17$ instead of 0.083, suggesting a preference for the TATT model.

Additionally, we analyse the 3×2-pt data vector with the dark-matter only version of HMCODE2020, which is a less accurate model for the non-linear matter power spectrum, since we know that baryonic feedback effects are not negligible. We find some shifts to lower values of S_8, within the error bars, which demonstrates that our scale cuts (validated in Emas et al. 2026) effectively mitigate the impact of mismodelling baryonic feedback in the non-linear matter power spectrum. Another evidence of this is the fact that the posterior distribution of $\log_{10}(T_{\rm AGN/K})$ is prior dominated (see Fig. 10), since we have removed the scales most sensitive to this parameter.

For the Monte Carlo chains in which we remove one lens bin at a time, we use an emulator for HMCODE2020 developed by Tsedrik et al. (2024) using COSMOPOWER (Spurio Mancini et al. 2022). We note that the emulator has a slightly narrower range allowed for the parameters $\Omega_{\rm m}$, $\sum m_\nu$, and $\log T_{\rm agn}$ with respect to our fiducial priors, which introduces

Table 6. Constraints on S_8 in ΛCDM assuming the TATT model for intrinsic alignments. We report the 68% credible intervals using the mean 1D marginal posterior distribution with the MAP estimate between parentheses. For each weak lensing dataset, we provide constraints from the 3×2-pt combination with DESI-DR1 projected galaxy clustering. Along with the marginalised constraints, we provide the Bayesian evidence ratio of TATT to NLA (R) and goodness of fit statistics: the χ^2 value at the best fit ($\chi^2_{\rm min}$), the estimated effective number of free parameters $N_{\rm p,eff}$, and the goodness of fit probability p (see Sec. 3.4 for more details).

WL survey	S_8	$R\,[\times10^{-2}]$	$\chi^2_{\rm min}$	$N_{\rm p,eff}$	$p(\chi^2_{\rm red})$
DES-Y3	$0.780^{+0.023}_{-0.021}$ (0.811)	7.2 ± 0.1	396.53	11.27	0.05
KiDS-1000	$0.731^{+0.023}_{-0.025}$ (0.735)	4901 ± 59	399.20	12.30	0.17
HSC-Y3	$0.767^{+0.028}_{-0.025}$ (0.769)	16.5 ± 0.2	246.24	13.91	0.76

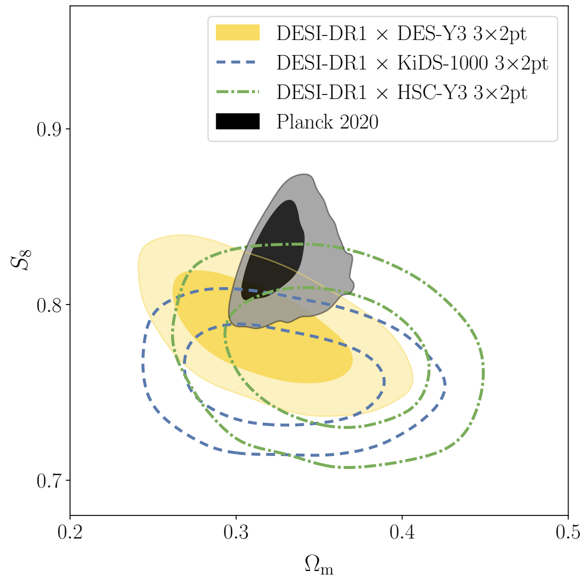

Figure 6. Marginalised constraints on $\Omega_{\rm m}$ and S_8 in ΛCDM from the 3×2-pt combination of DESI-DR1 projected galaxy clustering and weak lensing data from DES-Y3 (solid yellow), KiDS-1000 (dashed blue), and HSC-Y3 (dash-dotted green) compared to a re-analysis of the Planck Collaboration et al. (2020) CMB primary anisotropies with a common set of cosmological parameters and priors (solid black).

a slight shift to the constraints. We discuss and validate this comparison in Appendix C.

5. COMPARISON WITH PREVIOUS ANALYSES

In this section, we compare our main results in ΛCDM with previous results from each WL survey and with primary anisotropies from the Planck Collaboration et al. (2020) CMB observations, which have been reanalysed with a common set of priors. In particular, we include the primary temperature power spectra (TT) on scales $30\le\ell\le2508$, the E-mode and its cross power spectra with temperature (EE + TE) in the range $30\le\ell\le1996$, and the low-ℓ temperature and polarisation likelihood (TT + EE) at $2\le\ell\le29$.

In Fig. 6, we compare the S_8 and $\Omega_{\rm m}$ constraints from each 3×2-pt survey combination with the CMB primary anisotropies from Planck Collaboration et al. (2020). We find that our combined DESI-DR1 constraints using the WL data from DES-Y3, KiDS-1000, and HSC-Y3 are consistent with each other. To quantify the consistency with CMB observations from *Planck*, we estimate the parameter shift in the

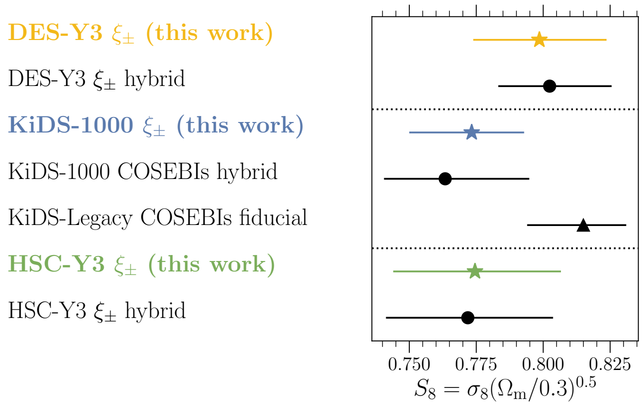

Figure 7. Marginalised constraints on S_8 in ΛCDM from the DES-Y3, KiDS-1000, and HSC-Y3 $\xi_\pm$ measurements used in this work compared with those obtained with the "*hybrid*" pipeline from DES and KiDS Collaboration (2023). Additionally, we compare with the recent KiDS-Legacy results from Wright et al. (2025).

$S_8-\Omega_{\rm m}$ plane using the TENSIOMETER package (see Sec. 3.4 for details), finding the following shift significance values,

$$\begin{array}{lll} \text{DESI-DR1} \times \text{DES-Y3} & \text{vs.} \quad \text{Planck}: & 1.3\sigma, \\ \text{DESI-DR1} \times \text{KiDS-1000} & \text{vs.} \quad \text{Planck}: & 2.1\sigma, \\ \text{DESI-DR1} \times \text{HSC-Y3} & \text{vs.} \quad \text{Planck}: & 1.4\sigma. \end{array} \tag{27}$$

We therefore do not conclude any statistical tension with early-Universe CMB observations, finding consistency at the $1.5-2\sigma$ level. While the cosmological constraints from each WL survey combination are consistent, a combined cosmic shear analysis would require a revalidation of the scale cuts at this increased precision (see, e.g., DES and KiDS Collaboration 2023). We therefore leave such combination for future work.

In Fig. 7, we compare our reanalysis of the cosmic shear $\xi_\pm$ measurements from DES-Y3, KiDS-1000, and HSC-Y3 with the corresponding constraints presented in DES and KiDS Collaboration (2023) using their "*hybrid*" pipeline, given that it is the most similar to the modelling choices assumed in our analysis. We additionally compare with the recent KiDS-Legacy cosmic shear results from Wright et al. (2025). For KiDS, we compare with their fiducial observable for cosmic shear, COSEBIs, instead of the real-space angular correlation functions $\xi_\pm$. The only differences between our modelling and inference pipeline and the *hybrid* pipeline are: (1) sampling of A_s, $\Omega_{\rm m}$ and $\Omega_{\rm b}$ instead of S_8, $\omega_{\rm c}$, and $\omega_{\rm b}$, (2) higher prior edge for $\log_{10}(T_{\rm AGN}/K)$ (8.3 instead of 8), (3) lower prior edge for the sum of neutrino masses (starting at 0 instead of 0.055 eV), (4) use of the NAUTILUS sampler instead of POLYCHORD (Handley et al. 2015). We find consistent S_8 constraints when analysing the same data set, with only small shifts in the reported mean values that are compatible with sampling variance. In general, the 68% credible intervals are slightly wider in our analysis due to the small change in priors, with the exception of KiDS-1000, for which we find smaller error bars than COSEBIs. The difference in constraining power in this case is due to having different scale sensitivities and a different degeneracy direction in the $\sigma_8-\Omega_{\rm m}$ plane. Asgari et al. (2021) found a similar difference of constraining power between COSEBIs and $\xi_\pm$ when reporting S_8 constraints. The fiducial cosmic shear constraints from KiDS-Legacy yield a higher value of S_8 (by $\sim2\sigma$) with respect to the KiDS-1000 constraints, bringing it closer to *Planck*. This

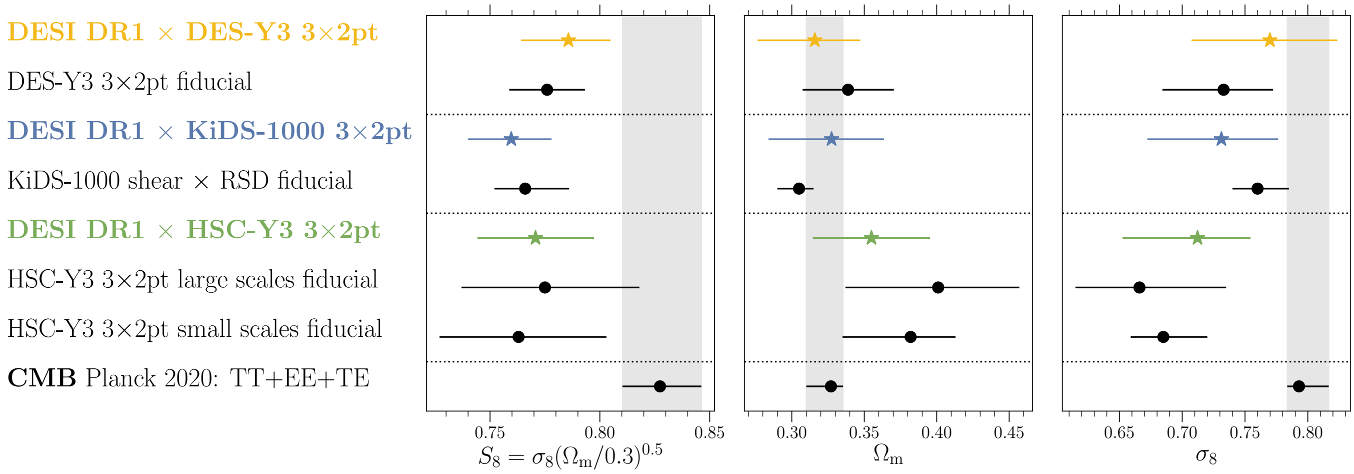

Figure 8. Marginalised constraints on S_8, Ω_m, and σ_8 in ΛCDM from the 3×2-pt combination of DESI-DR1 projected galaxy clustering and weak lensing data from DES-Y3, KiDS-1000, and HSC-Y3 compared to the corresponding fiducial results from each collaboration: DES Collaboration (2022) for DES-Y3, Heymans et al. (2021) for KiDS-1000, and Sugiyama et al. (2023) and Miyatake et al. (2023) for the HSC-Y3 large- and small-scale analyses, respectively. We also compare with a re-analysis of the Planck Collaboration et al. (2020) CMB primary anisotropies with a common set of cosmological parameters and priors.

difference is discussed in Sec. H.1 of Wright et al. (2025), where they conclude that it is mainly due to changes to the redshift calibration sample and methodology, besides the inclusion of new area in KiDS-Legacy.

In Fig. 8, we compare our 3×2-pt results from the combination of DESI-DR1 projected galaxy clustering and weak lensing data from DES-Y3, KiDS-1000, and HSC-Y3 with the fiducial results of each collaboration using a similar combination of probes. For DES-Y3, we compare with their fiducial 3×2-pt analysis from DES Collaboration (2022), which uses angular correlation functions $\{\xi_\pm(\theta),\, \gamma_t(\theta),\, w(\theta)\}$ and includes information from shear ratios (Sánchez, Prat et al. 2022) in the likelihood inference. Besides the addition of information from shear ratios, DES is the only survey out of the three that has carried out so far a 3×2-pt analysis using only internal data. Their galaxy-galaxy lensing measurements, therefore, cover the whole DES footprint and have much higher signal-to-noise ratio than in the other analyses, in which galaxy-galaxy lensing is limited to the overlapping area between the spectroscopic and WL surveys. Given the small overlapping area between DESI-DR1 and DES-Y3 (see Table 1 and Fig. 1 of Heydenreich et al. 2025), we do not find an improvement in constraining power with respect to the fiducial DES-Y3 3×2-pt analysis, even though we are using spectroscopic data for the projected galaxy clustering measurements.

For KiDS-1000 we do not have a comparable analysis in terms of observables, since their fiducial result from Heymans et al. (2021) uses redshift-space galaxy clustering from the Baryon Oscillation Spectroscopic Survey (BOSS), and additional spectroscopic data from the 2-degree Field Lensing Survey (2dFLenS) for the galaxy-galaxy lensing measurements. Their use of redshift-space galaxy clustering instead of projected galaxy clustering allows them to obtain much tighter constraints on Ω_m and σ_8, given that they have access to the full 3D information from spectroscopic galaxy clustering. Thus, it is not a fair comparison with our analysis. We refer the reader to our companion paper that uses full-shape modelling of the DESI-DR1 anisotropic galaxy clustering (Semenaite et al. 2025) for a comparison with KiDS-1000 on a more similar footing.

In the case of HSC-Y3 there are two fiducial 3×2-pt analyses, which use the Sloan Digital Sky Survey (SDSS) DR11 spectroscopic galaxy catalogue to measure projected galaxy clustering w_p and the galaxy-galaxy lensing observable $\Delta\Sigma$, i.e. the average excess surface mass density profile. Sugiyama et al. (2023) is the most similar to our analysis, since they also use a linear galaxy bias model and, therefore, restrict the analysis to the large scales. In particular, their scale cuts for galaxy-galaxy lensing and galaxy clustering are $(r_{p,\mathrm{ggl}},\, r_{p,\mathrm{clus}}) = (12,\, 8)\, h^{-1}\,\mathrm{Mpc}$, while we include scales up to $6\, h^{-1}\,\mathrm{Mpc}$ for galaxy-galaxy lensing thanks to the point-mass marginalisation[13]. Miyatake et al. (2023), instead, use the `Dark Emulator` (Nishimichi et al. 2019) to model the 2×2-pt observables to quasi-nonlinear scales, which allows them to increase the constraining power of the analysis.

From Fig. 8, we see that our 3×2-pt 1D marginalised constraints on S_8, Ω_m, and σ_8 in ΛCDM are consistent with the fiducial results from each WL survey, with differences smaller than 1σ. In this comparison, we were not expecting perfect consistency, given that we are using a new dataset for galaxy clustering from DESI-DR1. In addition to the potential statistical fluctuations from using new data, there are some differences in the modelling and analysis choices, scale cuts, and observables included, as summarised above.

6. CONCLUSIONS

We have presented cosmological constraints from a joint analysis of DESI-DR1 projected galaxy clustering with weak lensing data from DES-Y3 (Amon et al. 2022; Secco, Samuroff et al. 2022), KiDS-1000 (Asgari et al. 2021) and HSC-Y3 (Li et al. 2022), under a unified modelling and analysis pipeline.

We first reanalyse the cosmic shear $\xi_\pm$ measurements from these three WL datasets, finding highly consistent determinations of S_8 with those presented in DES and KiDS Collaboration (2023), see Fig. 7 for details. We then obtain cosmological constraints from the 2×2-pt combination of DESI-DR1 projected galaxy clustering with galaxy-galaxy lensing measured in the overlapping footprint with each WL dataset. After

[13] We note that the linear galaxy bias scale cuts for the DES-Y1 3×2-pt analysis, which did not include the point-mass marginalisation, were also $(r_{p,\mathrm{ggl}},\, r_{p,\mathrm{clus}}) = (12,\, 8)\, h^{-1}\,\mathrm{Mpc}$ (DES Collaboration 2018).

ensuring consistency between cosmic shear and 2×2-pt results, we combine them to obtain our final 3×2-pt constraints from these datasets.

In ΛCDM, we measure $S_8 = 0.786^{+0.022}_{-0.019}$ for DES-Y3 (2.6% precision), $S_8 = 0.760^{+0.020}_{-0.018}$ for KiDS-1000 (2.5% precision), and $S_8 = 0.771^{+0.026}_{-0.027}$ for HSC-Y3 (3.4% precision). These results are consistent with each other, across different weak lensing surveys, and also compatible with CMB observations from Planck Collaboration et al. (2020). We quantify the consistency with *Planck* at the $1.5 - 2\sigma$ level by means of parameter shift estimates in the $S_8 - \Omega_{\rm m}$ plane. We have validated that these 3×2-pt results are robust to several data splits and analysis variations in Sec. 4.3.

In wCDM, we measure the equation-of-state for dark energy to be $w = -1.12^{+0.32}_{-0.45}$ for the 3×2-pt combination with DES-Y3, $w = -0.88^{+0.18}_{-0.42}$ for KiDS-1000, and $w = -1.27^{+0.33}_{-0.40}$ for HSC-Y3. For all survey combinations, our results are consistent with the ΛCDM value, $w = -1$.

In Fig. 8 we compare our main ΛCDM 3×2-pt results with the corresponding fiducial ones from each WL survey, finding consistent constraints in general. Even though we are using spectroscopic galaxy clustering, and thus do not have to worry about photometric redshifts for the lenses, we still find some limitations in the constraining power due to: (1) the limited overlap between DESI-DR1 and the WL datasets, which lowers the signal-to-noise ratio of galaxy-galaxy lensing, (2) using projected galaxy clustering (2D) instead of anisotropic galaxy clustering measurements (3D information), (3) limitations in the modelling of the non-linear scales, which we do not include in our analysis. Nevertheless, some companion papers provide an improvement regarding the last two points. Semenaite et al. (2025) and DeRose et al. (2026) will provide complementary cosmological constraints using DESI-DR1 redshift-space galaxy clustering measurements instead of projected galaxy clustering, while Lange et al. (2025b) provides 2×2-pt cosmological constraints with a simulation-based approach that allows them to include smaller scales in the analysis.

In this work, we have used the cosmic shear measurements as provided by each WL collaboration, including their photometric redshift distributions and calibration. In the same way that we have unified the modelling and inference pipeline and the measurements of galaxy-galaxy lensing, one of the steps forward would be analysing these surveys under a unified photometric redshift calibration. Several companion papers have made advances in that regard: Lange et al. (2025a) perform an independent, unified photometric redshift calibration of DES-Y3, KiDS-1000 and HSC-Y1 source catalogues using the new DESI COSMOS-XMM catalog from Ratajczak et al. (2026), while Blanco et al. (2025) studies in more detail the potential for DESI to directly calibrate the KiDS-1000 source redshift distributions. In parallel, Ruggeri et al. (2025) provides estimates of the source redshift distributions of these WL datasets using clustering cross-correlation measurements with the DESI spectroscopic data.

All this work sets the ground for future combined analyses of weak lensing data with DESI Data Release 2 (DR2) spectroscopic galaxy clustering, which includes the first three years of main survey observations. In addition to the greater data quality of DESI-DR2, we expect to have a larger overlapping area with the northern region of the DES footprint. At the same time, cross-correlating DESI spectroscopic galaxy clustering with other WL datasets in the north, such as the Dark Energy Camera All Data Everywhere (DECADE) (Anbajagane et al. 2025a), the Ultraviolet Near-Infrared Optical Northern Survey (Gwyn et al. 2025), and the *Euclid* mission (Euclid Collaboration et al. 2025) in the future, will potentially increase the constraining power in a dramatic way. In this Stage-IV era of dark-energy surveys, it is critical to explore the synergies between different experiments and analyse them under a unified framework, to maximally exploit the wealth of information they provide, while assessing the robustness and consistency of different datasets.

ACKNOWLEDGMENTS

AP acknowledges financial support from the European Union's Marie Skłodowska-Curie grant agreement 101068581, and from the *César Nombela* Research Talent Attraction grant from the Community of Madrid (Ref. 2023-T1/TEC-29011). CB and NE acknowledge financial support from Australian Research Council Discovery Project DP220101609, and NE acknowledges financial support received through a Swinburne University Postgraduate Research Award.

This material is based upon work supported by the U.S. Department of Energy (DOE), Office of Science, Office of High-Energy Physics, under Contract No. DE–AC02–05CH11231, and by the National Energy Research Scientific Computing Center, a DOE Office of Science User Facility under the same contract. Additional support for DESI was provided by the U.S. National Science Foundation (NSF), Division of Astronomical Sciences under Contract No. AST-0950945 to the NSF's National Optical-Infrared Astronomy Research Laboratory; the Science and Technology Facilities Council of the United Kingdom; the Gordon and Betty Moore Foundation; the Heising-Simons Foundation; the French Alternative Energies and Atomic Energy Commission (CEA); the National Council of Humanities, Science and Technology of Mexico (CONAHCYT); the Ministry of Science, Innovation and Universities of Spain (MICIU/AEI/10.13039/501100011033), and by the DESI Member Institutions: https://www.desi.lbl.gov/collaborating-institutions. Any opinions, findings, and conclusions or recommendations expressed in this material are those of the author(s) and do not necessarily reflect the views of the U. S. National Science Foundation, the U. S. Department of Energy, or any of the listed funding agencies.

The authors are honored to be permitted to conduct scientific research on I'oligam Du'ag (Kitt Peak), a mountain with particular significance to the Tohono O'odham Nation.

This work was supported through computational resources and services provided by the National Energy Research Scientific Computing Center (NERSC), a U.S. Department of Energy Office of Science User Facility operated under Contract No. DE-AC02-05CH11231. We also acknowledge the use of Spanish Supercomputing Network (RES) resources provided by the Barcelona Supercomputing Center (BSC) in MareNostrum 5 under allocations 2025-1-0045 and 2025-2-0046.

This research made use of the following python packages in addition to those already cited in the manuscript: ASTROPY (Astropy Collaboration et al. 2022), NUMPY (Harris et al. 2020), SCIPY (Virtanen et al. 2020) and MATPLOTLIB (Hunter 2007).

DATA AVAILABILITY

Data points for the figures are available at https://doi.org/10.5281/zenodo.17937581.

REFERENCES

Aihara H., et al., 2022, PASJ, 74, 247
Amon A., et al., 2022, Phys. Rev. D, 105, 023514
Anbajagane D., et al., 2025a, The Open Journal of Astrophysics, 8, 46158
Anbajagane D., et al., 2025b, The Open Journal of Astrophysics, 8, 46161
Asgari M., et al., 2021, A&A, 645, A104
Astropy Collaboration et al., 2022, ApJ, 935, 167
Bianchi D., et al., 2025, J. Cosmology Astropart. Phys., 2025, 074
Bigwood L., et al., 2024, MNRAS, 534, 655
Blake C., et al., 2025, The Open Journal of Astrophysics, 8, 24
Blanco D., et al., 2025, arXiv e-prints, p. arXiv:2512.15964
Blazek J. A., MacCrann N., Troxel M. A., Fang X., 2019, Phys. Rev. D, 100, 103506
Bridle S., King L., 2007, New Journal of Physics, 9, 444
Brown M. L., Taylor A. N., Hambly N. C., Dye S., 2002, MNRAS, 333, 501
Cai Y.-C., Bernstein G., 2012, MNRAS, 422, 1045
Chaussidon E., et al., 2023, ApJ, 944, 107
Chen S., et al., 2024, Phys. Rev. D, 110, 103518
Choppin de Janvry J., Gontcho S. G. A., Seljak U., Baleato Lizancos A., Chaussidon E., et al., 2025a, arXiv e-prints, p. arXiv:2511.18133
Choppin de Janvry J., Dai B., Gontcho S. G. A., Seljak U., Zhang T., 2025b, arXiv e-prints, p. arXiv:2511.18134
Cole S., Fisher K. B., Weinberg D. H., 1994, MNRAS, 267, 785
Cross D. N., Sánchez C., 2024, Phys. Rev. D, 110, 123534
DES Collaboration 2018, Phys. Rev. D, 98, 043526
DES Collaboration 2022, Phys. Rev. D, 105, 023520
DES and KiDS Collaboration 2023, The Open Journal of Astrophysics, 6, 36
DESI Collaboration et al., 2016a, arXiv e-prints, p. arXiv:1611.00036
DESI Collaboration et al., 2016b, arXiv e-prints, p. arXiv:1611.00037
DESI Collaboration et al., 2022, AJ, 164, 207
DESI Collaboration et al., 2024, AJ, 167, 62
DESI Collaboration et al., 2025a, Phys. Rev. D, 112, 083514
DESI Collaboration et al., 2025b, Phys. Rev. D, 112, 083515
DESI Collaboration et al., 2025c, J. Cosmology Astropart. Phys., 2025, 021
DESI Collaboration et al., 2025d, J. Cosmology Astropart. Phys., 2025, 017
DESI Collaboration et al., 2025e, J. Cosmology Astropart. Phys., 2025, 028
DESI Collaboration et al., 2026, AJ, 171, 285
Dalal R., et al., 2023, Phys. Rev. D, 108, 123519
DeRose J., et al., 2023, J. Cosmology Astropart. Phys., 2023, 054
DeRose J., et al., 2026, (in prep.)
Dey A., et al., 2019, AJ, 157, 168
Di Valentino E., et al., 2021, Classical and Quantum Gravity, 38, 153001
Elvin-Poole J., MacCrann N., et al., 2023, MNRAS, 523, 3649
Emas N., et al., 2026, The Open Journal of Astrophysics, 9, 59886
Euclid Collaboration et al., 2025, A&A, 697, A1
Fang X., Krause E., Eifler T., MacCrann N., 2020a, JCAP, 05, 010
Fang X., Eifler T., Krause E., 2020b, MNRAS, 497, 2699
Fenech Conti I., Herbonnet R., Hoekstra H., Merten J., Miller L., Viola M., 2017, MNRAS, 467, 1627
Flaugher B., et al., 2015, AJ, 150, 150
Freedman W. L., 2021, ApJ, 919, 16
Friedrich O., et al., 2021, MNRAS, 508, 3125
García-García C., Zennaro M., Aricò G., Alonso D., Angulo R. E., 2024, J. Cosmology Astropart. Phys., 2024, 024
Gatti M., et al., 2021, MNRAS, 504, 4312
Gaztañaga E., Eriksen M., Crocce M., Castander F. J., Fosalba P., Marti P., Miquel R., Cabré A., 2012, MNRAS, 422, 2904
Giblin B., et al., 2021, A&A, 645, A105
Guy J., et al., 2023, AJ, 165, 144
Gwyn S., et al., 2025, AJ, 170, 324
Hadzhiyska B., et al., 2023, MNRAS, 526, 369
Hahn C., et al., 2023, AJ, 165, 253
Hamana T., et al., 2020, PASJ, 72, 16
Handley W. J., Hobson M. P., Lasenby A. N., 2015, MNRAS, 450, L61
Harris C. R., et al., 2020, Nature, 585, 357
Heydenreich S., et al., 2025, arXiv e-prints, p. arXiv:2506.21677
Heymans C., et al., 2021, A&A, 646, A140
Hikage C., et al., 2019, PASJ, 71, 43
Hildebrandt H., et al., 2017, MNRAS, 465, 1454
Hildebrandt H., et al., 2020, A&A, 633, A69
Hildebrandt H., et al., 2021, A&A, 647, A124
Hirata C. M., Seljak U., 2004, Phys. Rev. D, 70, 063526
Hirata C. M., Mandelbaum R., Ishak M., Seljak U., Nichol R., Pimbblet K. A., Ross N. P., Wake D., 2007, MNRAS, 381, 1197
Hunter J. D., 2007, CiSE, 9, 90
Huterer D., 2023, A&A Rev., 31, 2
Ishak M., 2019, Living Reviews in Relativity, 22, 1
Jefferson J., et al., 2025, The Open Journal of Astrophysics, 8, 139
Jeffreys H., 1935, Proceedings of the Cambridge Philosophical Society, 31, 203
Joachimi B., Bridle S. L., 2010, A&A, 523, A1
Joachimi B., et al., 2021, A&A, 646, A129
Joudaki S., et al., 2018, MNRAS, 474, 4894
Kaiser N., 1987, MNRAS, 227, 1
Karamanis M., Beutler F., 2021, arXiv e-prints, p. arXiv:2106.06331
Kirk D., Lahav O., Bridle S., Jouvel S., Abdalla F. B., Frieman J. A., 2015, MNRAS, 451, 4424
Krause E., Eifler T., 2017, MNRAS, 470, 2100
Krause E., et al., 2021, arXiv e-prints, p. arXiv:2105.13548
Kuijken K., et al., 2019, A&A, 625, A2
Lamman C., Tsaprazi E., Shi J., Šarčević N. N., Pyne S., Legnani E., Ferreira T., 2024, The Open Journal of Astrophysics, 7, 14
Lange J. U., 2023, MNRAS, 525, 3181
Lange J., Huang S., 2022, dsigma: Galaxy-galaxy lensing Python package, Astrophysics Source Code Library, record ascl:2204.006 (ascl:2204.006)
Lange J. U., et al., 2025a, arXiv e-prints, p. arXiv:2510.25419
Lange J. U., et al., 2025b, arXiv e-prints, p. arXiv:2512.15962
Leauthaud A., et al., 2017, MNRAS, 467, 3024
Lewis A., 2025, J. Cosmology Astropart. Phys., 2025, 025
Lewis A., Challinor A., Lasenby A., 2000, ApJ, 538, 473
Li X., et al., 2022, PASJ, 74, 421
Li X., et al., 2023, Phys. Rev. D, 108, 123518
Limber D. N., 1953, ApJ, 117, 134
LoVerde M., Afshordi N., 2008, Phys. Rev. D, 78, 123506
MacCrann N., Blazek J., Jain B., Krause E., 2020, MNRAS, 491, 5498
MacCrann N., et al., 2022, MNRAS, 509, 3371
Mandelbaum R., et al., 2018, PASJ, 70, S25
McCarthy I. G., Schaye J., Bird S., Le Brun A. M. C., 2017, MNRAS, 465, 2936
McCullough J., et al., 2024, arXiv e-prints, p. arXiv:2410.22272
Mead A. J., Brieden S., Tröster T., Heymans C., 2021, MNRAS, 502, 1401
Miller L., et al., 2013, MNRAS, 429, 2858
Miller T. N., et al., 2024, AJ, 168, 95
Miyatake H., et al., 2023, Phys. Rev. D, 108, 123517
Modi C., Chen S.-F., White M., 2020, MNRAS, 492, 5754
Moresco M., et al., 2022, Living Reviews in Relativity, 25, 6
Muir J., et al., 2020, MNRAS, 494, 4454
Myles J., et al., 2021, MNRAS, 505, 4249
Nishimichi T., et al., 2019, ApJ, 884, 29
Pandey S., et al., 2022, Phys. Rev. D, 106, 043520
Planck Collaboration Aghanim N., et al., 2020, A&A, 641, A6
Poppett C., et al., 2024, AJ, 168, 245
Porredon A., et al., 2022, Phys. Rev. D, 106, 103530
Raichoor A., et al., 2023, AJ, 165, 126
Rana D., More S., Miyatake H., Sugiyama S., Zhang T., Shirasaki M., 2026, Phys. Rev. D, 113, 063534
Ratajczak J., et al., 2026, AJ, 171, 71
Rau M. M., et al., 2023, MNRAS, 524, 5109
Raveri M., Doux C., 2021, Phys. Rev. D, 104, 043504
Raveri M., Hu W., 2019, Phys. Rev. D, 99, 043506
Reischke R., et al., 2025, A&A, 699, A124
Riess A. G., et al., 2016, ApJ, 826, 56
Riess A. G., et al., 2022, ApJL, 934, L7
Ruggeri R., et al., 2025, arXiv e-prints, p. arXiv:2512.15963
Sánchez C., Prat J., et al., 2022, Phys. Rev. D, 105, 083529
Schlafly E. F., et al., 2023, AJ, 166, 259
Secco L. F., Samuroff S., et al., 2022, Phys. Rev. D, 105, 023515
Semenaite A., et al., 2025, arXiv e-prints, p. arXiv:2512.15961
Sevilla-Noarbe I., et al., 2021, ApJS, 254, 24
Sheldon E. S., Huff E. M., 2017, ApJ, 841, 24
Shirasaki M., Takada M., 2018, MNRAS, 478, 4277
Silber J. H., et al., 2023, AJ, 165, 9
Sinha M., Garrison L. H., 2020, MNRAS, 491, 3022
Spurio Mancini A., Piras D., Alsing J., Joachimi B., Hobson M. P., 2022, MNRAS, 511, 1771
Stebbins A., 1996, arXiv e-prints, pp astro–ph/9609149
Sugiyama S., et al., 2023, Phys. Rev. D, 108, 123521

Takada M., Hu W., 2013, Phys. Rev. D, 87, 123504
Troxel M. A., Ishak M., 2015, Phys. Rep., 558, 1
Troxel M. A., et al., 2018, MNRAS, 479, 4998
Tsedrik M., Bose B., Carrilho P., Pourtsidou A., Pamuk S., Casas S., Lesgourgues J., 2024, J. Cosmology Astropart. Phys., 2024, 099
Vagnozzi S., 2023, Universe, 9, 393
Virtanen P., et al., 2020, Nature Methods, 17, 261
Weinberg D. H., Mortonson M. J., Eisenstein D. J., Hirata C., Riess A. G., Rozo E., 2013, Phys. Rep., 530, 87
Wright A. H., et al., 2025, A&A, 703, A158
Yuan S., et al., 2024, MNRAS, 533, 589
Zhang T., et al., 2023, MNRAS, 525, 2441
Zhang T., et al., 2025, arXiv e-prints, p. arXiv:2507.01386
Zhou R., et al., 2023, AJ, 165, 58
Zuntz J., et al., 2015, Astronomy and Computing, 12, 45
de Putter R., Doré O., Takada M., 2013, arXiv e-prints, p. arXiv:1308.6070
van Daalen M. P., McCarthy I. G., Schaye J., 2020, MNRAS, 491, 2424

AFFILIATIONS

[1] CIEMAT, Avenida Complutense 40, E-28040 Madrid, Spain
[2] Institute for Astronomy, University of Edinburgh, Royal Observatory, Blackford Hill, Edinburgh EH9 3HJ, UK
[3] Ruhr University Bochum, Faculty of Physics and Astronomy, Astronomical Institute (AIRUB), German Centre for Cosmological Lensing, 44780 Bochum, Germany
[4] The Ohio State University, Columbus, 43210 OH, USA
[5] Centre for Astrophysics & Supercomputing, Swinburne University of Technology, P.O. Box 218, Hawthorn, VIC 3122, Australia
[6] Department of Physics, American University, 4400 Massachusetts Avenue NW, Washington, DC 20016, USA
[7] Lawrence Berkeley National Laboratory, 1 Cyclotron Road, Berkeley, CA 94720, USA
[8] Department of Physics, Boston University, 590 Commonwealth Avenue, Boston, MA 02215 USA
[9] Department of Physics, The University of Texas at Dallas, 800 W. Campbell Rd., Richardson, TX 75080, USA
[10] Dipartimento di Fisica "Aldo Pontremoli", Università degli Studi di Milano, Via Celoria 16, I-20133 Milano, Italy
[11] INAF-Osservatorio Astronomico di Brera, Via Brera 28, 20122 Milano, Italy
[12] Department of Physics & Astronomy, University College London, Gower Street, London, WC1E 6BT, UK
[13] Institut d'Estudis Espacials de Catalunya (IEEC), c/ Esteve Terradas 1, Edifici RDIT, Campus PMT-UPC, 08860 Castelldefels, Spain
[14] Institute of Space Sciences, ICE-CSIC, Campus UAB, Carrer de Can Magrans s/n, 08913 Bellaterra, Barcelona, Spain
[15] Instituto de Astrofísica de Canarias, C/ Vía Láctea, s/n, E-38205 La Laguna, Tenerife, Spain
[16] Department of Physics and Astronomy, The University of Utah, 115 South 1400 East, Salt Lake City, UT 84112, USA
[17] Instituto de Física, Universidad Nacional Autónoma de México, Circuito de la Investigación Científica, Ciudad Universitaria, Cd. de México C. P. 04510, México
[18] Department of Astronomy & Astrophysics, University of Toronto, Toronto, ON M5S 3H4, Canada
[19] Department of Physics & Astronomy and Pittsburgh Particle Physics, Astrophysics, and Cosmology Center (PITT PACC), University of Pittsburgh, 3941 O'Hara Street, Pittsburgh, PA 15260, USA
[20] Department of Physics, The Ohio State University, 191 West Woodruff Avenue, Columbus, OH 43210, USA
[21] University of California, Berkeley, 110 Sproul Hall #5800 Berkeley, CA 94720, USA
[22] Institut de Física d'Altes Energies (IFAE), The Barcelona Institute of Science and Technology, Edifici Cn, Campus UAB, 08193, Bellaterra (Barcelona), Spain
[23] Departamento de Física, Universidad de los Andes, Cra. 1 No. 18A-10, Edificio Ip, CP 111711, Bogotá, Colombia
[24] Observatorio Astronómico, Universidad de los Andes, Cra. 1 No. 18A-10, Edificio H, CP 111711 Bogotá, Colombia
[25] Center for Astrophysics | Harvard & Smithsonian, 60 Garden Street, Cambridge, MA 02138, USA
[26] NASA Einstein Fellow
[27] Institute of Cosmology and Gravitation, University of Portsmouth, Dennis Sciama Building, Portsmouth, PO1 3FX, UK
[28] University of Virginia, Department of Astronomy, Charlottesville, VA 22904, USA
[29] Fermi National Accelerator Laboratory, PO Box 500, Batavia, IL 60510, USA
[30] Institute of Astronomy, University of Cambridge, Madingley Road, Cambridge CB3 0HA, UK
[31] Institut d'Astrophysique de Paris. 98 bis boulevard Arago. 75014 Paris, France
[32] IRFU, CEA, Université Paris-Saclay, F-91191 Gif-sur-Yvette, France
[33] Department of Astronomy and Astrophysics, UCO/Lick Observatory, University of California, 1156 High Street, Santa Cruz, CA 95064, USA
[34] Center for Cosmology and AstroParticle Physics, The Ohio State University, 191 West Woodruff Avenue, Columbus, OH 43210, USA
[35] School of Mathematics and Physics, University of Queensland, Brisbane, QLD 4072, Australia
[36] Department of Physics, University of Michigan, 450 Church Street, Ann Arbor, MI 48109, USA
[37] University of Michigan, 500 S. State Street, Ann Arbor, MI 48109, USA
[38] NSF NOIRLab, 950 N. Cherry Ave., Tucson, AZ 85719, USA
[39] Department of Physics and Astronomy, University of California, Irvine, 92697, USA
[40] Department of Physics and Astronomy, University of Waterloo, 200 University Ave W, Waterloo, ON N2L 3G1, Canada
[41] Perimeter Institute for Theoretical Physics, 31 Caroline St. North, Waterloo, ON N2L 2Y5, Canada
[42] Waterloo Centre for Astrophysics, University of Waterloo, 200 University Ave W, Waterloo, ON N2L 3G1, Canada
[43] Sorbonne Université, CNRS/IN2P3, Laboratoire de Physique Nucléaire et de Hautes Energies (LPNHE), FR-75005 Paris, France
[44] Department of Astronomy and Astrophysics, University of California, Santa Cruz, 1156 High Street, Santa Cruz, CA 95065, USA
[45] Departament de Física, Serra Húnter, Universitat Autònoma de Barcelona, 08193 Bellaterra (Barcelona), Spain
[46] Institució Catalana de Recerca i Estudis Avançats, Passeig de Lluís Companys, 23, 08010 Barcelona, Spain
[47] Departamento de Física, DCI-Campus León, Universidad de Guanajuato, Loma del Bosque 103, León, Guanajuato C. P. 37150, México
[48] Instituto Avanzado de Cosmología A. C., San Marcos 11 - Atenas 202. Magdalena Contreras. Ciudad de México C. P. 10720, México
[49] Space Sciences Laboratory, University of California, Berkeley, 7 Gauss Way, Berkeley, CA 94720, USA
[50] Instituto de Astrofísica de Andalucía (CSIC), Glorieta de la Astronomía, s/n, E-18008 Granada, Spain
[51] Departament de Física, EEBE, Universitat Politècnica de Catalunya, c/Eduard Maristany 10, 08930 Barcelona, Spain
[52] Department of Physics and Astronomy, Sejong University, 209 Neungdong-ro, Gwangjin-gu, Seoul 05006, Republic of Korea
[53] Queensland University of Technology, School of Chemistry & Physics, George St, Brisbane 4001, Australia
[54] Max Planck Institute for Extraterrestrial Physics, Gießenbachstraße 1, 85748 Garching, Germany
[55] Department of Physics & Astronomy, Ohio University, 139 University Terrace, Athens, OH 45701, USA
[56] National Astronomical Observatories, Chinese Academy of Sciences, A20 Datun Road, Chaoyang District, Beijing, 100101, P. R. China

APPENDIX

A. HSC YEAR 1

We have also carried out a 3×2-pt analysis using HSC Year 1 (Y1) data (Mandelbaum et al. 2018), given that this survey combination was validated in the "*mock-challenge*"

Table 7. HSC-Y1 constraints on S_8, Ω_m, and σ_8 in ΛCDM and on w in wCDM, with 68% credible intervals using the mean 1D marginal posterior distribution. We report constraints on HSC-Y1 cosmic shear, the combination of DESI-DR1 projected galaxy clustering and galaxy-galaxy lensing (2×2-pt), and the full 3×2-pt data vector. Along with the marginalised constraints, we provide goodness of fit statistics: the χ^2 value at the best fit ($\chi^2_{\rm min}$), the total number of data points $N_{\rm D}$, the estimated effective number of free parameters $N_{\rm p,eff}$, the reduced $\chi^2_{\rm red} = \chi^2_{\rm min}/(N_{\rm D} - N_{\rm p,eff})$, and the goodness of fit probability p (see Sec. 3.4 for more details).

Analysis	S_8	$\Omega_{\rm m}$	σ_8	w	$\chi^2_{\rm min}$	$N_{\rm D}$	$N_{\rm p,eff}$	$\chi^2_{\rm red}$	$p(\chi^2_{\rm red})$
ΛCDM									
Cosmic shear	$0.858^{+0.028}_{-0.032}$	$0.304^{+0.090}_{-0.041}$	$0.872^{+0.110}_{-0.122}$	-	201.52	170	4.59	1.22	0.029
2×2-pt	$0.695^{+0.117}_{-0.109}$	$0.343^{+0.048}_{-0.049}$	$0.654^{+0.129}_{-0.106}$	-	159.20	137	9.13	1.25	0.031
3×2-pt	$0.849^{+0.025}_{-0.027}$	$0.318^{+0.049}_{-0.033}$	$0.829^{+0.070}_{-0.059}$	-	362.64	307	10.62	1.22	0.005
wCDM									
3×2-pt	$0.864^{+0.039}_{-0.048}$	$0.325^{+0.048}_{-0.037}$	$0.835^{+0.074}_{-0.064}$	$-0.88^{+0.15}_{-0.43}$	361.35	307	10.77	1.22	0.006

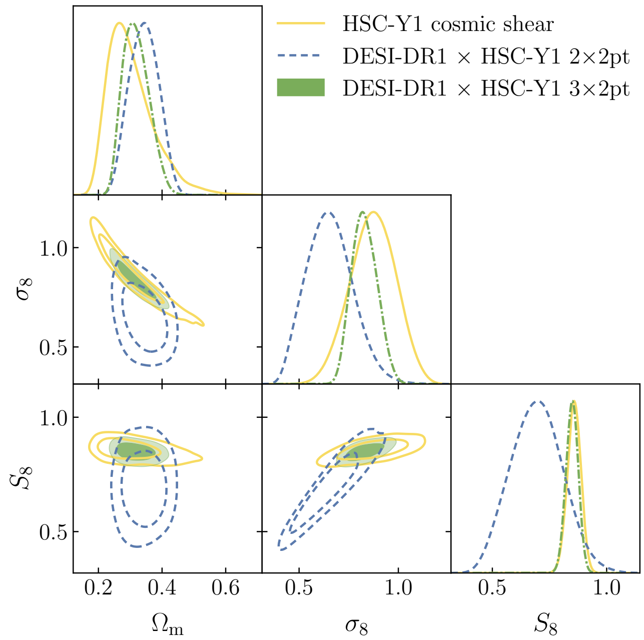

Figure 9. Marginalised constraints on Ω_m, σ_8, and S_8 in ΛCDM for HSC-Y1 cosmic shear (solid yellow), the combination of galaxy-galaxy lensing and projected galaxy clustering from DESI-DR1 (dashed blue), and the 3×2-pt combination (solid green).

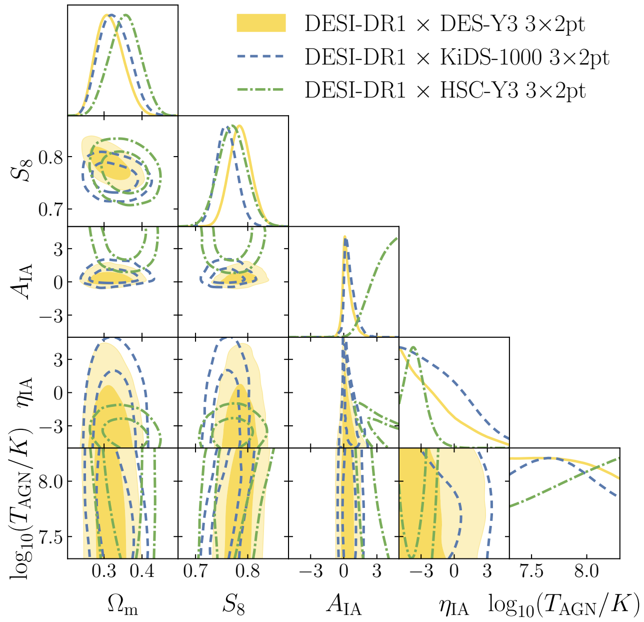

Figure 10. Marginalised constraints on Ω_m, S_8, and the IA and baryonic feedback parameters in ΛCDM from the 3×2-pt combination of DESI-DR1 projected galaxy clustering and weak lensing data from DES-Y3 (solid yellow), KiDS-1000 (dashed blue), and HSC-Y3 (dash-dotted green).

paper by Blake et al. (2025) and was also considered in the other supporting papers, such as Heydenreich et al. (2025) and Emas et al. (2026). In this case, the overlapping area with DESI-DR1 is 151.8 deg^2. We follow the fiducial HSC-Y1 cosmic shear analyses (Hikage et al. 2019; Hamana et al. 2020) to set the Gaussian priors on the data-calibration nuisance parameters. For shear calibration, these priors are the same as those for HSC-Y3 in Table 2. Regarding photometric-redshift uncertainties, HSC-Y1 also assumes a Gaussian prior on the Δz^j of each source bin j, centered at zero, and with $\sigma(\Delta z^j) = [0.0374, 0.0124, 0.0326, 0.0343]$. In this case, there are also two parameters that correct for PSF-related systematics, $\alpha_{\rm PSF}$ and $\beta_{\rm PSF}$. The corresponding Gaussian priors are $(0.029, 0.01)$ and $(-1.42, 1.11)$, respectively, where we have expressed the Gaussian prior of the form $\mathcal{N}(\mu, \sigma)$.

In Table 7, we report the 68% credible intervals around the mean 1D marginal posterior for the main cosmological parameters (S_8, Ω_m, σ_8, and w), along with the goodness of fit metrics for each probe combination and cosmological model (ΛCDM and wCDM). While the goodness-of-fit p value for cosmic shear and 2×2-pt is above our threshold ($p > 0.01$), this is not the case for the 3×2-pt combinations. This is probably due to the high S_8 value preferred by the HSC Y1 $\xi_{+/-}$ cosmic shear constraints, which is considerably higher than the constraint from the 2×2-pt part of the data vector. The fiducial HSC Y1 cosmic shear constraints in real space (see Hamana et al. 2020 after the erratum correction) are somewhat in tension with the harmonic space analysis from Hikage et al. (2019) ($\sim 1.6\sigma$ higher in S_8), which might indicate some unknown systematic with the data. We also note that the HSC Y1 footprint is small with many holes (see Fig. 1 from Mandelbaum et al. 2018), which makes it more challenging to have an accurate analytical covariance matrix. For this reason, we report these constraints for completeness, but do not include them in the main results of this paper. In Fig. 9, we show the marginalised posterior distributions for Ω_m, S_8, and σ_8 in ΛCDM.

B. ADDITIONAL POSTERIOR DISTRIBUTIONS

In this Section, we include additional marginalised posterior distributions for the main 3×2-pt analyses in ΛCDM presented in this work. Fig. 10 shows the posterior distributions of S_8 and Ω_m, together with the IA NLA and baryonic feedback parameters. We find that the DESI-DR1 3×2-pt combinations with DES Y3 and KiDS-1000 are able to con-

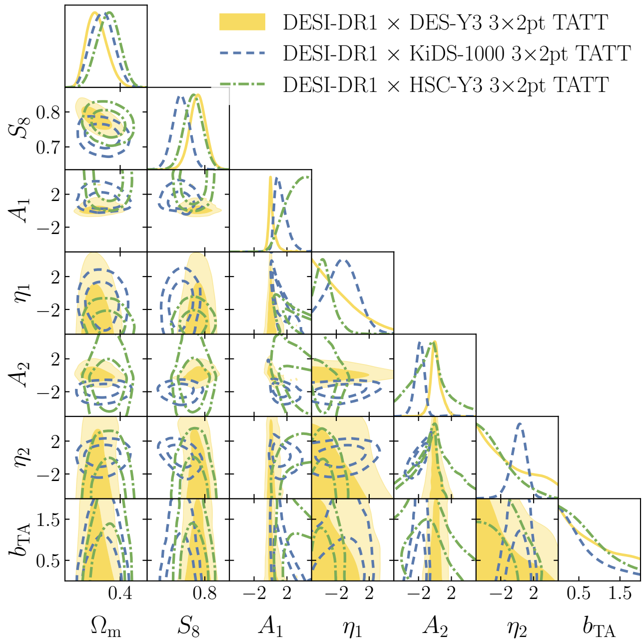

Figure 11. Marginalised constraints on Ω_m, S_8 and the IA parameters from the TATT model, in ΛCDM from the 3×2-pt combination of DESI-DR1 projected galaxy clustering and weak lensing data from DES-Y3 (solid yellow), KiDS-1000 (dashed blue), and HSC-Y3 (dash-dotted green).

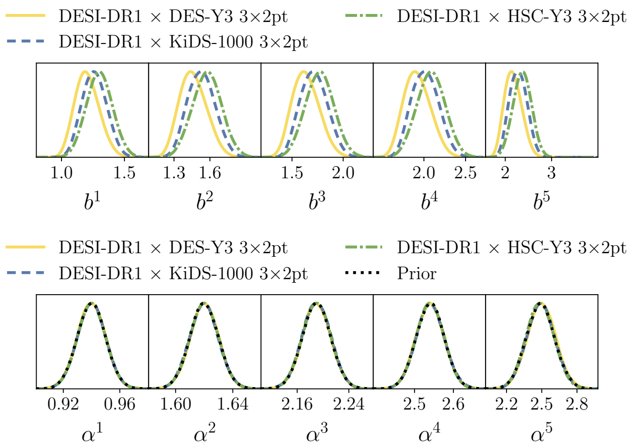

Figure 12. Marginalised constraints on the galaxy bias (top) and lens magnification (bottom) parameters, in ΛCDM, from the 3×2-pt combination of DESI-DR1 projected galaxy clustering and weak lensing data from DES-Y3 (solid yellow), KiDS-1000 (dashed blue), and HSC-Y3 (dash-dotted green). The priors assumed for the lens magnification parameters (see Table 1) are included in dotted black lines.

strain the amplitude of intrinsic alignments from our fiducial NLA model. However, the combination with HSC Y3 seems unable to constrain these parameters, which hit the edge of the priors. This is probably due to the wide flat priors assumed for Δ_z^3 and Δ_z^4, which the data has to self-calibrate. As a consequence, there is not enough constraining power to constrain the amplitude of intrinsic alignments A_IA. The parameter $\log_{10}(T_\mathrm{AGN}/K)$ is in general unconstrained, since we have removed the scales most sensitive to baryonic feedback through the scale cuts validated in Emas et al. (2026). Similarly, in Fig. 11, we show the marginalised posterior distributions when using the TATT model for intrinsic alignments, where we find that the 3×2-pt combination with KiDS-1000 is able to constrain some of the additional IA parameters, like A_2 and η_2.

In Fig. 12, we compare the 1D marginalised posterior distributions on the galaxy bias and lens magnification parameters. The lens magnification parameters are not constrained by the data, and therefore we find that they agree perfectly with the Gaussian priors assumed (see Table 1). The galaxy bias posterior distributions, as expected, are consistent among the different survey combinations, since all the analyses share the same DESI-DR1 lenses.

In Fig. 13, we present the 1D marginalised posterior distributions of most of the shear nuisance parameters assumed for DES-Y3, HSC-Y3, and KiDS-1000. We also overlay the Gaussian priors assumed for these parameters (see Table 2). We find that the data is able to constrain some of these parameters (especially the Δ_z ones). In all cases, we find consistency between these posterior distributions and the priors assumed (as required by our unblinding requirements).

In Fig. 14, we show the marginalised posterior distributions of the IA and Δ_z parameters of the DESI-DR1 × HSC-Y3 3×2-pt analysis in ΛCDM. We do not find any degeneracy or strong correlation between the IA and photometric redshift parameters. Additionally, we see that the data is able to constrain the parameters Δ_z^3 and Δ_z^4, which have very wide flat priors instead of Gaussian ones (see Table 2).

C. VALIDATION OF HMCODE2020 EMULATOR

As mentioned in Sec. 4.3, we use the HMCODE2020 emulator developed by Tsedrik et al. (2024) using COSMOPOWER (Spurio Mancini et al. 2022) to test the robustness of our results by excluding one lens redshift bin at a time. The parameter ranges of this emulator are narrower than those of our fiducial priors from Table 1 on the Ω_m, Σm_ν, and $\log_{10}(T_\mathrm{AGN}/K)$ parameters. We therefore tighten the priors on these parameters to match the emulator's range in those cases, in the following way: (1) the higher edge prior of Ω_m is reduced to 0.8 instead of 0.9, (2) the higher edge prior of Σm_ν is reduced to 0.5 instead of 0.6, and (3) the lower edge prior for $\log_{10}(T_\mathrm{AGN}/K)$ is increased to 7.6 instead of 7.3.

This change in priors slightly shifts the constraints on cosmological parameters. Fig. 15 shows the marginalised constraints on the Ω_m, σ_8, and S_8 cosmological parameters from the DES-Y3 3×2-pt analysis using our fiducial pipeline compared to the HMCODE2020 emulator. The difference in the 1D mean marginals in these parameters are 0.06σ, 0.12σ and 0.2σ, respectively. These shifts are small enough to enable the use of the emulator for the robustness tests in Sec. 4.3 and open the door to using it to accelerate future analyses.

This paper was built using the Open Journal of Astrophysics LaTeX template. The OJA is a journal which provides fast and easy peer review for new papers in the `astro-ph` section of the arXiv, making the reviewing process simpler for authors and referees alike. Learn more at `http://astro.theoj.org`.

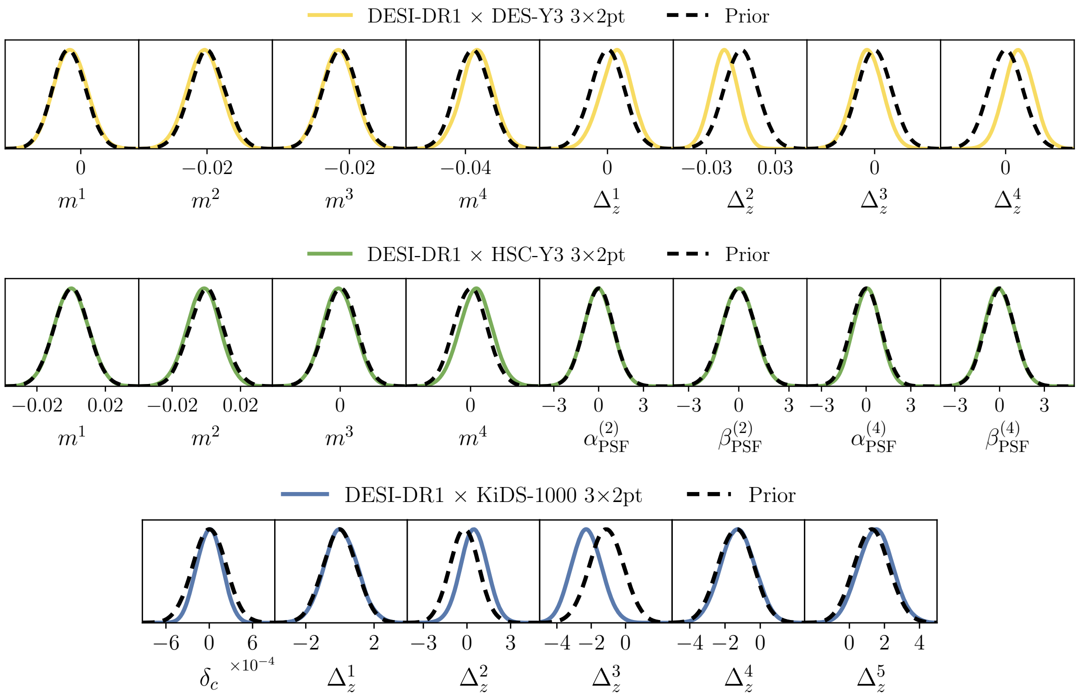

Figure 13. 1D marginalised constraints on the shear nuisance parameters from the 3 × 2-pt combination of DESI-DR1 projected galaxy clustering and weak lensing data from DES-Y3 (top), HSC-Y3 (middle), and KiDS-1000 (bottom). The priors assumed for these parameters (see Table 2) are included in dashed black lines.

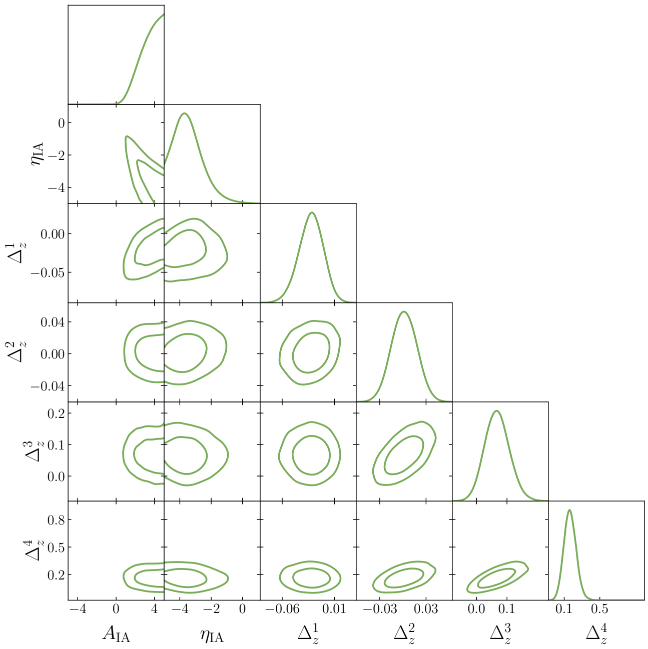

Figure 14. Marginalised constraints on the IA and Δ_z parameters, in ΛCDM, from the 3×2-pt combination of DESI-DR1 projected galaxy clustering and HSC-Y3 weak lensing data.

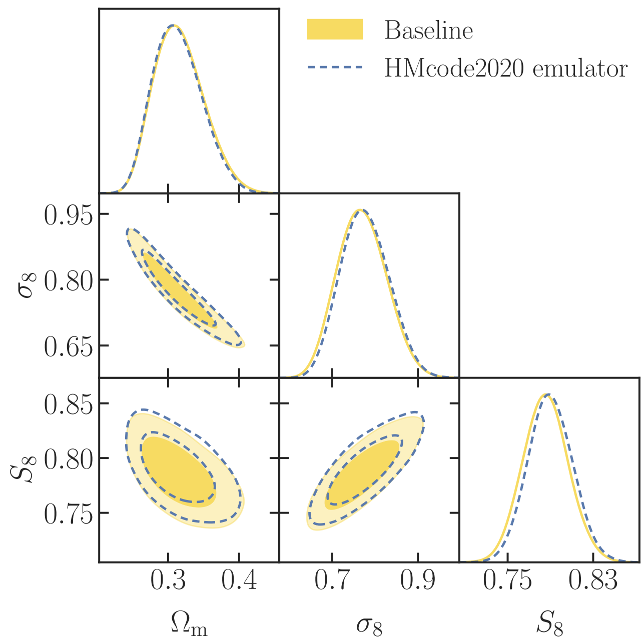

Figure 15. Comparison between the marginalised constraints on the parameters $\Omega_{\rm m}$, σ_8, and S_8 from the baseline DESI-DR1 × DES-Y3 3×2-pt combined analysis (solid yellow) to a similar analysis using the HMCODE2020 emulator (dashed blue).